

# Energy & Environmental Science

Accepted Manuscript



This is an *Accepted Manuscript*, which has been through the Royal Society of Chemistry peer review process and has been accepted for publication.

*Accepted Manuscripts* are published online shortly after acceptance, before technical editing, formatting and proof reading. Using this free service, authors can make their results available to the community, in citable form, before we publish the edited article. We will replace this *Accepted Manuscript* with the edited and formatted *Advance Article* as soon as it is available.

You can find more information about *Accepted Manuscripts* in the [Information for Authors](#).

Please note that technical editing may introduce minor changes to the text and/or graphics, which may alter content. The journal's standard [Terms & Conditions](#) and the [Ethical guidelines](#) still apply. In no event shall the Royal Society of Chemistry be held responsible for any errors or omissions in this *Accepted Manuscript* or any consequences arising from the use of any information it contains.

**Progress in triboelectric nanogenerators as new energy technology and self-powered sensors†**

Cite this: *Energy Environ. Sci.*, 2015, 00, 1-10.

Zhong Lin Wang,<sup>\*ab</sup> Jun Chen,<sup>a</sup> Long Lin<sup>a</sup>

Received 0th January 2014,  
Accepted 0th January 2014

DOI: 10.1039/x0xx00000x

www.rsc.org/ees

Ever since the first report of the triboelectric nanogenerator (TENG) in January 2012, its output area power density reaches  $500 \text{ W m}^{-2}$ , an instantaneous conversion efficiency of  $\sim 70\%$  and total energy conversion efficiency of up to  $85\%$  have been demonstrated. We provide a comprehensive review about the four modes, their theoretical modelling, and the applications of TENGs for harvesting energy from human motion, walking, vibration, mechanical triggering, rotating tire, wind, flowing water and more as well as self-powered sensors.

**Broader context**

Using the electrostatic charges created on the surfaces of two dissimilar materials when they are brought into physical contact, the contact induced triboelectric charges can generate a potential drop when the two surfaces are separated by a mechanical force, which can drive electrons to flow between the two electrodes built on the top and bottom surfaces of the two materials. This is the triboelectric nanogenerator (TENG). Ever since the first report of the TENG in January 2012 by Wang *et al.*, its output area power density reaches  $500 \text{ W m}^{-2}$ , an instantaneous conversion efficiency of  $\sim 70\%$  and total energy conversion efficiency of up to  $85\%$  have been demonstrated. This article provides a comprehensive review about the four modes of the TENGs, their theoretical modelling, and the applications of TENGs for harvesting energy from human motion, walking, vibration, mechanical triggering, rotating tire, wind, flowing water and more. A TENG can also be used as a self-powered sensor for actively detecting the static and dynamic processes arising from mechanical agitation using the voltage and current output signals of the TENG, respectively, with potential applications as mechanical sensors and for touch pad and smart skin technologies. The potential of TENG for harvesting ocean wave energy is also discussed as a potential approach for the blue energy by harvesting ocean wave energy at an estimated power density of  $1.15 \text{ MW km}^{-2}$ .

**1. Introduction****1.1 Background of energy harvesting**

Energy is one of the most important resources that dictates the quality of our life. With the limited fossil energy for the next century, searching for new energy has been a major challenge facing today's society. The most familiar renewable energies are solar, wind and tide energy, which are targeted to contribute to the major power grid to meet the need of mega- to giga-watt power scale. The general requirements for harvesting these types of energies are low-cost, high stability and high efficiency.

In the last two decades, the vast applications and distributions of mobile electronics have reached every corner of our life. Vast types of sensors for health monitoring, medical care, environmental protection, infrastructure monitoring and security. The power for

driving each unit is small and can be down to mille-even micro-Watt range, but the number of units can be huge. As predicted by Cisco, by 2020 the world will have trillions of sensor units distributed on the earth.<sup>1</sup> The recent development of internet of things (IoT) and sensor networks dramatically change the traditional understanding about energy. The general characteristics of this type of power units are mobility, availability and sustainability. The most conventional technology is using battery, which may not be the solution for IoT. For trillions of batteries that are vastly distributed and each has limited life time, monitoring, replacing, recycling and exchanging batteries would be a huge and even impossible task. Most of the IoT would be impossible without making the devices self-powered.<sup>2</sup> It is thus desirable to integrate an energy harvester together with a battery to form a self-powered system is likely to be an ideal choice. This was the background for the birth of nanogenerators, a revolutionary

approach toward nanoenergy.<sup>3</sup>

## 1.2 Nanogenerators

Today's electronics is mostly associated with human activities for the purpose of health, safety and communication. The most abundant energy associated with a human is mechanical energy as a result of body motion. Nanogenerator was first introduced to harvest human energy from walking, talking, breathing, typing and more utilizing

two effects: piezoelectricity<sup>4-9</sup> and triboelectricity.<sup>10-12</sup> Using the strain induced piezoelectric polarization in certain crystals, such as ZnO and PZT, the potential created by polarization charges can drive the flow of electrons across two electrodes placed on the top and bottom surfaces of the crystal. This is the general principle of piezoelectric nanogenerators (PENG). We have spent the last 10 years in developing the PENG, which has been reported systematically in existing literatures.<sup>13-18</sup>

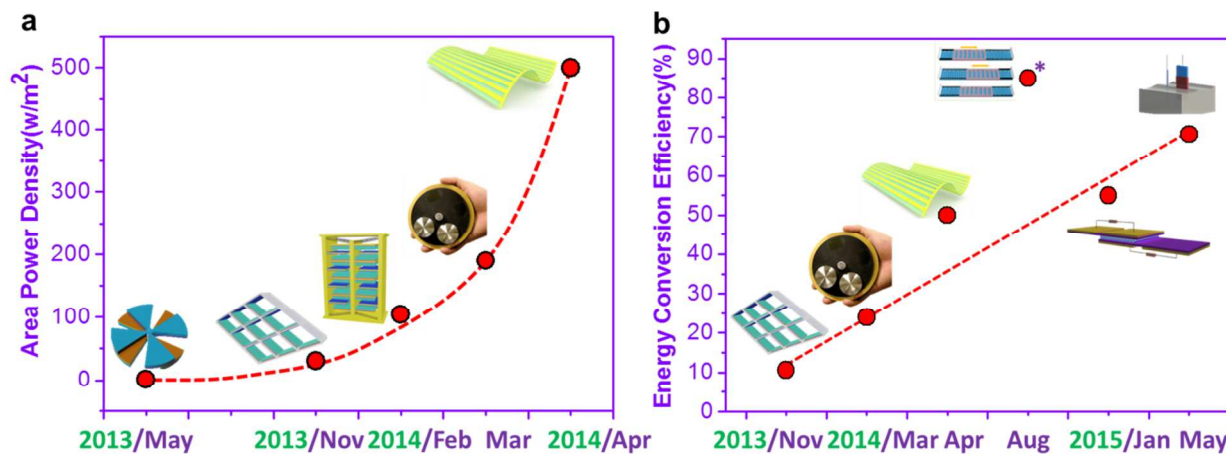


**Fig. 1** Summary on the progress in the performance of TENG made in the (a) area output power density and (b) energy conversion efficiency within the last 12 months. In May 2015, an instantaneous energy conversion efficiency of  $\sim 70\%$  has been demonstrated using liquid metal as a contact material. For low frequency agitation and if the energy generated by all the residual vibrations are acquired, a total energy conversion efficiency of up to  $85\%$  has been shown experimentally in August of 2014. \*: total energy conversion efficiency; the rest of data are instantaneous energy conversion efficiency.

Most recently, using the electrostatic charges created on the surfaces of two dissimilar materials when they are brought into physical contact, the contact induced triboelectric charges can generate a potential drop when the two surfaces are separated by mechanical force, which can drive electrons to flow between the two electrodes built on the top and bottom surfaces of the two materials. This is the birth of the triboelectric nanogenerator (TENG).<sup>19</sup> Ever since the first report of the TENG in January 2012, the area power density reaches  $500 \text{ Wm}^{-2}$ ,<sup>20</sup> volume power density reaches  $15 \text{ MWm}^{-3}$ ,<sup>20</sup> and an instantaneous conversion efficiency of  $\sim 70\%$  has been demonstrated (Fig. 1).<sup>21</sup> For low frequency agitation and if the energy generated by all the residual vibrations are acquired, a total energy conversion efficiency of up to  $85\%$  has been shown experimentally.<sup>22</sup> The TENG can be applied to harvest all kinds of mechanical energies that are available but wasted in our daily life, such as human motion, walking, vibration, mechanical triggering, rotating tire, wind, flowing water and more.<sup>23</sup> Alternatively, a TENG

can also be used as a self-powered sensor for actively detecting the static and dynamic processes arising from mechanical agitation using the voltage and current output signals of the TENG, respectively, with potential applications as mechanical sensors and for touch pad and smart skin technologies.<sup>24</sup> The TENG also has the potential of harvesting wave energy in ocean based on a new approach, which could be a new paradigm for large scale energy.<sup>25,26</sup> Based on the existing reviews on TENGs,<sup>23-26</sup> this article covers the updated progress in TENG both as a power source and as self-powered sensor.

## 2. Four fundamental working modes of the TENG

Triboelectrification is an effect that is known to each and every one probably ever since the ancient Greek time, but it is usually taken as a negative effect and is avoided in many technologies. Discharges caused by triboelectricity have many disaster damages to industrial processes, electronics, human life and nature, such as wild fire. But this effect exists almost everywhere in our life and for any

materials we use each day, so that it is not limited to any specific materials. Our goal here is to use triboelectricity for converting mechanical energy into electricity based on new materials and new designs.

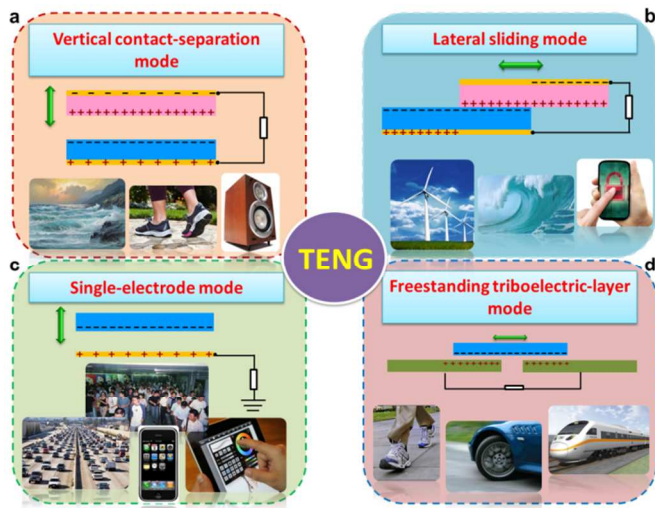


**Fig. 2** The four fundamental working modes of the triboelectric nanogenerators. (a) The vertical contact-separation mode. (b) The lateral sliding mode. (c) The single-electrode mode. (d) The free-standing mode. Reproduced with permission from the Royal Society of Chemistry.<sup>25</sup>

As for TENG, in the open-circuit condition, a potential difference between two electrodes attached on the back sides of the films is created by the coupling of triboelectrification and electrostatic induction. The triboelectric charges are generated due to the charge transfer between two thin organic/inorganic films that exhibit distinct surface electron affinity, and the potential difference results from the separation of the triboelectric charges; in the short-circuit condition, electrons are driven to flow between two electrodes attached on the back sides of the films through the load to balance the potential difference resulted from mechanical action. Here we first introduce the four fundamental modes of the TENG, which are the basics for various prototypes of the TENGs.<sup>25</sup>

### 2.1 Vertical contact-separation mode.

The vertical contact-separation mode was the first invented operation mode for the TENGs.<sup>27-29</sup> A physical contact between the two dielectric films with distinct electron affinity (at least one is insulative) creates oppositely charged surfaces. Once the two surfaces are separated by a gap, a potential drop is created between electrodes deposited on the top and the bottom surfaces of two dielectric films, as demonstrated in Fig. 2a. If the two electrodes are

electrically connected by a load, free electrons in one electrode would flow to the other electrode in order to balance the electrostatic field. Once the gap is closed, the potential drop created by the triboelectric charges disappears, the induced electrons will flow back. A periodic contact and separation between the two materials drives the induced electrons to flow back and forth between the two electrodes, resulting in an AC output in the external circuit.

In this mode, the electricity generation process depends on a periodic switching between the contact and separation states of the two contact surfaces, and the output is AC. To realize this type of mechanical motion, various structural designs were developed, including arch-shaped,<sup>28</sup> spring-supported,<sup>30,31</sup> zig-zag,<sup>32,33</sup> cantilever based,<sup>34</sup> and so on. The TENGs based on this working mode excels in cyclic motions, intermittent impact or shock. This mode was featured as simple structure design, great device robustness, and high instantaneous power density. However, an indispensable design of the vertical contact-separation mode is a cavity with constantly changing volume, which renders a challenge for the packaging of the TENG.

The vertical contact-separation mode has been widely used to harvest energy from finger typing,<sup>35</sup> engine vibration,<sup>31</sup> human walking,<sup>33,36,37</sup> biomedical system.<sup>38</sup> And it was also developed to build up self-powered sensor systems, including magnetic sensor,<sup>39</sup> pressure sensor,<sup>40</sup> vibration sensor,<sup>31</sup> mercury ion sensor,<sup>41</sup> catechin detection sensor,<sup>42</sup> acoustic sensors<sup>43,44</sup>.

### 2.2 In-plane sliding mode.

As shown in Fig. 2b, when two materials with opposite triboelectric polarities, for instance, PTFE and aluminum, are brought into contact, surface charge transfer takes place due to the triboelectrification effect. Since PTFE holds a higher electron affinity than aluminum, electrons are injected from aluminum into PTFE. When the PTFE and Al are fully aligned, the electric field created by the triboelectric charges does not produce a potential drop, because the positive charges on aluminum are fully compensated by the negative ones on PTFE. Once a relative displacement is introduced by an externally applied force in the direction parallel to the interface, triboelectric charges are not fully compensated at the displaced/mismatched areas, resulting in the creation of an effective dipole polarization in parallel to the direction of the displacement. Therefore, a potential difference across the two electrodes is generated. A sliding back and forth between the two will result in a periodical change of the electric potential difference, which will

drive free electrons to flow alternatively across the electrodes.<sup>45, 46</sup>

The in-plane sliding mode holds several important advantages compared to the vertical contact-separation mode. The generation of triboelectric charges from the relative sliding between two surfaces is much more effective than the pure contact, which contributes to a greatly enhanced output power for practical applications.<sup>46</sup> And furthermore, the in-plane sliding mode is easy to develop more advanced design for high-performance TENGs. For instance, through a grating structure, the total transported charge is greatly enhanced.<sup>20,45,47</sup> With constant sliding velocity, finer grating shortens the time to transport induced charges between the electrodes, which enables substantial enhancements of both the magnitude and frequency of the output current.

The in-plane sliding mode excels in harvesting energy from planar motions,<sup>45,46,48</sup> disc rotation<sup>49,50</sup> and cylindrical rotation.<sup>51</sup> And it was demonstrated to harvest wind energy,<sup>52</sup> hydropower,<sup>53</sup> rotational kinetic energy,<sup>49</sup> and so on. And it was also developed to function as a motion sensor,<sup>54</sup> velocity sensor,<sup>55</sup> and so on.

### 2.3 Single-electrode mode.

For both the vertical contact-separation mode and in-plane sliding mode triboelectric nanogenerators, the moving objects need to be bonded with an electrode and a lead wire. Such a device configuration largely limits TENGs' versatility and applicability for harvesting energy from an arbitrary, freely moving object, because the object has to be connected to the entire system by an interconnect. A single electrode mode TENG was developed to solve this problem.<sup>56</sup> As demonstrated in Fig. 2c, which consists of, for instance, a PTFE moving object and an aluminum layer electrically connected to the ground. In the original position, PTFE and aluminum are fully in contact with each other, which will result in that electrons are injected from aluminum to PTFE since PTFE has higher surface electron affinity than aluminum. Once the negatively charged PTFE slides apart or separates, a decrease of the induced positive charges on the Al occurs, and the electrons will flow from ground to aluminum till the two plates are entirely separated, in order to balance the electric potential. Then, when the PTFE slides backward or comes to contact again, the induced positive charges on the aluminum increase, driving the electrons to flow from aluminum to the ground till the two plates fully overlapped to re-establish an electrostatic equilibrium. This is a full cycle of electricity generation process of the single-electrode mode TENG.

In the single electrode mode, although the induced electrons

transfer across the electrode is not the best effectiveness due to the electrostatic screening effect,<sup>57</sup> one of the triboelectric layers can move freely without any restriction. With this unique feature, the single electrode mode has been applied to harvest energy from air flow,<sup>58</sup> rotating tire,<sup>59</sup> rain drop,<sup>60</sup> turning the book pages.<sup>61</sup> And it was also applied as self-powered displacement vector sensor,<sup>56</sup> visualized touch sensor,<sup>62</sup> active tactile sensor,<sup>63,64</sup> self-powered trajectory, velocity sensor,<sup>65,66</sup> angle measurement sensor,<sup>67</sup> acceleration sensors,<sup>68</sup> biosensor,<sup>69</sup> water/ethanol sensor,<sup>70</sup> pressure sensor,<sup>71</sup> sensor for healthcare monitoring,<sup>72</sup> body motion sensors,<sup>73,74</sup> self-powered identification systems,<sup>75</sup> and self-powered distress signal emitter.<sup>76</sup>

### 2.4 Free-standing triboelectric-layer mode.

The freestanding triboelectric-layer mode triboelectric nanogenerator is also capable of scavenging energy from the mechanical motion without an attached electrode,<sup>77</sup> as shown in Fig. 2d. If we make a pair of symmetric electrodes underneath a dielectric layer and the size of the electrodes are of the same order as the size of the moving object, and there is a small gap between the object and the electrode, the object's approaching to and/or departing from the electrodes create an asymmetric charge distribution via induction in the media, provided the object was prior-charged by a triboelectric process, which causes the electrons to flow between the two electrodes to balance the local potential distribution. The oscillation of the electrons between the paired electrodes in responding to the back and forth motion of the object produces an AC current output.

Compared to the single-electrode mode, there is no screening effect in this mode, and the electrostatically-induced electron transfer can reach the same amount of the triboelectric charges on the free-standing layer. In this working mode, there is no direct physical contact between the two triboelectric layers, compared to the in-plane sliding mode, it will cause no material abrasion and heat generation under long-term continuous working.<sup>78</sup> This distinguishes the free-standing mode with ultra-robustness as well as high energy conversion efficiency. This freestanding triboelectric-layer mode TENG has been demonstrated to harvest energy from vibration,<sup>79</sup> rotation motions,<sup>80,81</sup> computer mouse operation,<sup>82</sup> air flow,<sup>83</sup> a walking human or a moving automobile.<sup>22,77</sup> And it was developed into self-powered vibration sensor<sup>79</sup> and active micro-actuators.<sup>84</sup>

## 3. Fundamental theory of the TENGs

### 3.1 Fundamental theories of various working modes of the TENGs

This section will systematically review the theory and physical models for various TENGs. The theories will provide the fundamental understanding and guidance for optimizing device performance with advanced structural design and materials usage, as well as suitable system-level topologies for integrated energy harvesting systems. To investigate the physics behind the TENGs, the first step was to classify the TENGs as different modes from their fundamental electrostatic induction process.

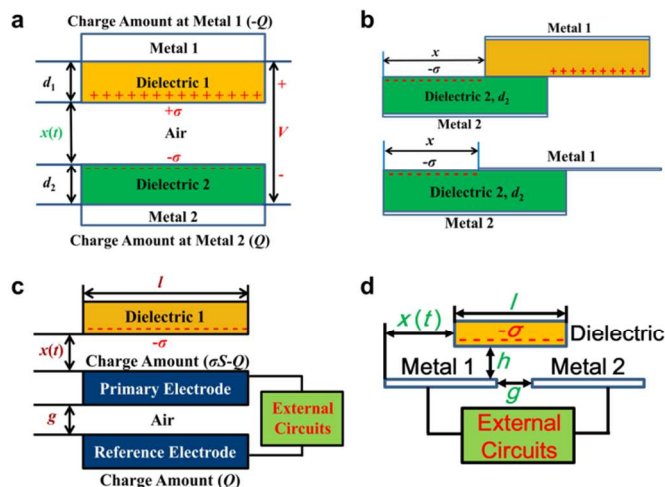


**Fig. 3** Fundamental theories of four working modes of the TENGs. (a) The mode built for a dielectric-to-dielectric contact-mode TENG.<sup>85</sup> (b) The theoretical models for the dielectric-to-dielectric (up) and metal-to-dielectric (bottom) sliding mode TENG.<sup>86</sup> (c) The theoretical models for the single electrode mode TENG.<sup>57</sup> (d) The theoretical models of the sliding-mode freestanding TENG.<sup>87</sup>

The theoretical models for the four kinds of TENGs were respectively illustrated in Fig. 3. The model built for a dielectric-to-dielectric contact-mode TENG is shown in Fig. 3a.<sup>85</sup> Basically, two dielectric plates, with thickness of  $d_1$  and  $d_2$  and relative dielectric constants  $\epsilon_{r1}$  and  $\epsilon_{r2}$ , respectively, are stacked face to face as two triboelectric layers. Two metal layers are deposited as two electrodes. The gap distance  $x$  between the two triboelectric layers can be periodically changed due to the external mechanical force. When the external force brings the two dielectric materials to contact, the inner surface of the two triboelectric layers will have opposite static charges with equal density of  $\sigma$  due to the contact electrification. When the external force separates the two mutually charged surfaces, an electric potential difference  $V$  between the two electrodes will be induced. The changing  $V$  will drive the electrons to flow back and forth across the electrodes. And the amount of transferred charges between the two electrodes is defined as  $Q$ . And the governing  $V$ - $Q$ - $x$  relationship and intrinsic output characteristic

of the vertical contact separation model can be expressed as

$$V = -\frac{Q}{S\epsilon_0}(d_0 + x(t)) + \frac{\sigma x(t)}{\epsilon_0} \quad (1)$$

where  $d_0$  is the effective dielectric thickness, and  $\epsilon_0$  is the dielectric constant of vacuum.

Figure 3b shows the theoretical models for the dielectric-to-dielectric (up) and metal-to-dielectric (bottom) sliding mode TENG.<sup>86</sup> In this mode, two metal electrodes are still bonded with the dielectric layers. The bottom part is fixed while the top can slide through the longitudinal direction. And the lateral separation distance is defined as  $x$ . When the top metal or dielectric layer is sliding apart, there are charges with different signs at the non-overlapped regions. For the metal-to-dielectric mode, the top metal layer plays dual roles as an electrode and a triboelectric layer. The analytical equation for the general case of sliding-mode TENGs cannot be derived and rigorous theoretical analysis can only base on numerical simulations. The  $V$ - $Q$ - $x$  relationship for the sliding mode TENGs by neglecting the edge effect can be expressed as:

$$V = -\frac{d_0}{W\epsilon_0(l-x)}Q + \frac{\sigma d_0 x}{\epsilon_0(l-x)} \quad (2)$$

Figure 3c shows the theoretical models for the single electrode mode TENG. Here, we just take the metal-to-dielectric contact case as an example to illustrate its physical picture.<sup>57</sup> A dielectric plate and a metal electrode are stacked face to face to form a triboelectric pair, with the same length  $l$  and width of  $w$ . And the thickness is  $d_1$  for dielectric 1 and  $d_m$  for the primary electrode. A gap of  $g$  was set between the primary electrode and reference electrode, which holds identical geometric size. To operate, the two electrodes are fixed and dielectric 1 can move along the vertical direction under the external mechanical excitation. Basically, the output performance of the single electrode mode TENG is limited by the electrostatic shield effect of their primary electrodes.

Figure 3d is the theoretical model of the dielectric sliding-mode freestanding TENG.<sup>87</sup> Metal 1 and 2 are placed in a same plane with a gap  $g$ , acting as the two electrodes. A freestanding dielectric layer with the same size of electrode stands on the top of the metal electrode with a vertical distance  $h$ , namely, the freestanding height. The width of this structure is defined as  $w$ . In this mode, the dielectric bottom surface cannot be seen as a single node, since its electrical potential is not a constant. Here, it is assumed that only a small region of  $dk$  in the bottom dielectric surface contains the tribo-charges with a density of  $\sigma$ , and the total charges on the two electrodes are  $\sigma wdk$ . Thus, the total charges on the two electrodes,  $dQ_1$  and  $dQ_2$  under short-circuit conditions can be expressed as:

$$dQ_1 = \frac{\sigma w d k}{1 + \frac{C_2(k)}{C_1(k)}} \quad (3)$$

$$dQ_2 = \frac{\sigma w d k}{1 + \frac{C_1(k)}{C_2(k)}} \quad (4)$$

where  $C_i(k)$  represents the capacitance between surface  $\sigma w d k$  and metal  $i$ . In this working mode, the change of  $x$  is the core-working principle of the dielectric sliding-mode freestanding TENG.

### 3.2 Theoretical investigations on the structural optimizations of TENGs

In this section, a review of the influence of several important structural parameters on the output performance of TENG will be presented, based on which some optimization strategies are proposed to obtain an improved output performance.

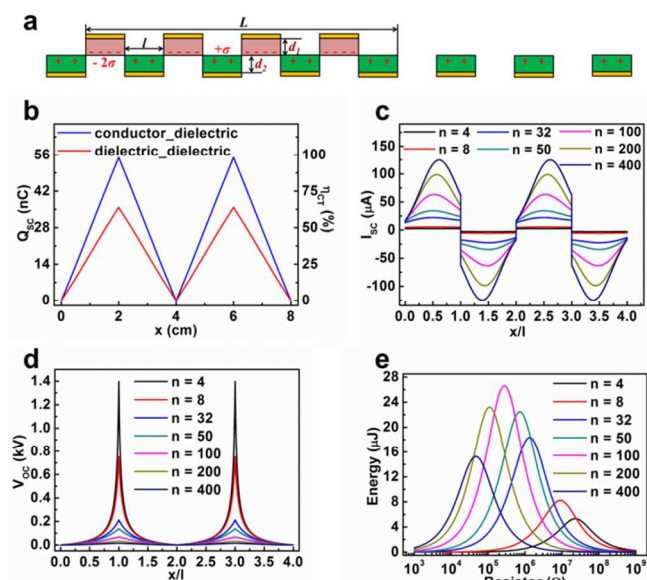


**Fig. 4** Theoretical investigations on the structural optimizations of TENG.<sup>88</sup> (a) The finite element method model for the grating structure with unequal-length plates. (b) The comparison of conductor-to-dielectric and dielectric-to-dielectric unequal-length grating TENGs on short circuit transferred charges. (c) With increasing the grating units, the short-circuit current is obviously increased. (d) With increasing the grating units, the open-circuit voltage is decreased. (e) The relationship of the total harvested energy with the load resistance. Reproduced with permission from the Royal Society of Chemistry.

A typical characteristic of the TENG is high output voltage but low current. In order to enhance the total output current at the expenses of the output voltage, grating structure is an effective and advanced design, which is mainly attributed to the multiplied charge separation cycles in a grating structure. Fig. 4a shows a finite element

method model for the grating structure with unequal-length plates.<sup>88</sup> In the model, the length of the bottom part is set to  $2L$ , which is twice the length of the top part. Thus, the tribo-charge density of dielectric 1 ( $-2\sigma$ ) is twice as high as that of the dielectric 2 ( $\sigma$ ).  $d_1$  and  $d_2$  are respectively the thickness of dielectric layer 1 and 2, respectively.  $l$  is the separation between gratings. To begin with, the dielectric thickness shows impact on the grating structure TENG. With increase the ratio of the  $d_2/d_1$ , both the short circuit transferred charges ( $Q_{sc}$ ) and the charge transfer efficiency ( $\eta_{CT}$ ) decrease dramatically. Fig. 4b is a comparison of conductor-to-dielectric and dielectric-to-dielectric unequal-length grating TENGs on short circuit transferred charges.<sup>88</sup> As it shows, the peak values of  $Q_{sc}$  and  $\eta_{CT}$  from the conductor-to-dielectric TENG are higher than the dielectric-to-dielectric TENG, which indicates that the conductor-to-dielectric design is more preferable for the efficient charge transfer. Furthermore, the influence of the grating units is systematically investigated. As shown in Fig. 4c, with increasing of the grating units, the short-circuit current is obviously increased, while the open-circuit voltage follows a reverse trend, as demonstrated in Fig. 4d. Still, the load performance of the grating TENGs is numerically calculated. Fig. 4e shows the relationship of the total harvested energy with the load resistance. And the optimum resistance shifts significantly to lower values since finer pitches yield a larger inherent TENG capacitance. To summarize, structural parameters, including the dielectric thickness, number of grating units, shows significant impact on the TENG output performance.

### 3.3 Theoretical investigations on the energy harvesting system based on TENGs

TENG as an energy harvesting technology, its resistive load characteristics are critically important for the performance evaluation. And the equivalent circuit of the whole system is presented in Fig. 5a. Here, the contact-separation model TENG is taken as an example and two cases are respectively considered.

The first case is the resistive output characteristics when the TENG is separated at a uniform velocity.<sup>89, 90</sup> And the numerical calculated peak values of the voltage and current on different loads are shown in Fig. 5b. It clearly demonstrates that the operation of the TENG can be divided into three working regions. In the first region, the resistance is low and in a range of 0.1 to 1000  $\Omega$ , and the peak current shows little drop compared with that in the short-circuit condition. In the region 2, the peak current drops dramatically while the peak voltage increases following an inverse trend. In the region 3,

where the external resistance is usually larger than 1 G $\Omega$ . The output voltage is close to and saturated at that of the open-circuit condition.

instantaneous power output, which indicates that the maximum output power was obtained at a matched external resistance around 100 M $\Omega$ .

Figure 5c shows the influence of the load resistance on the

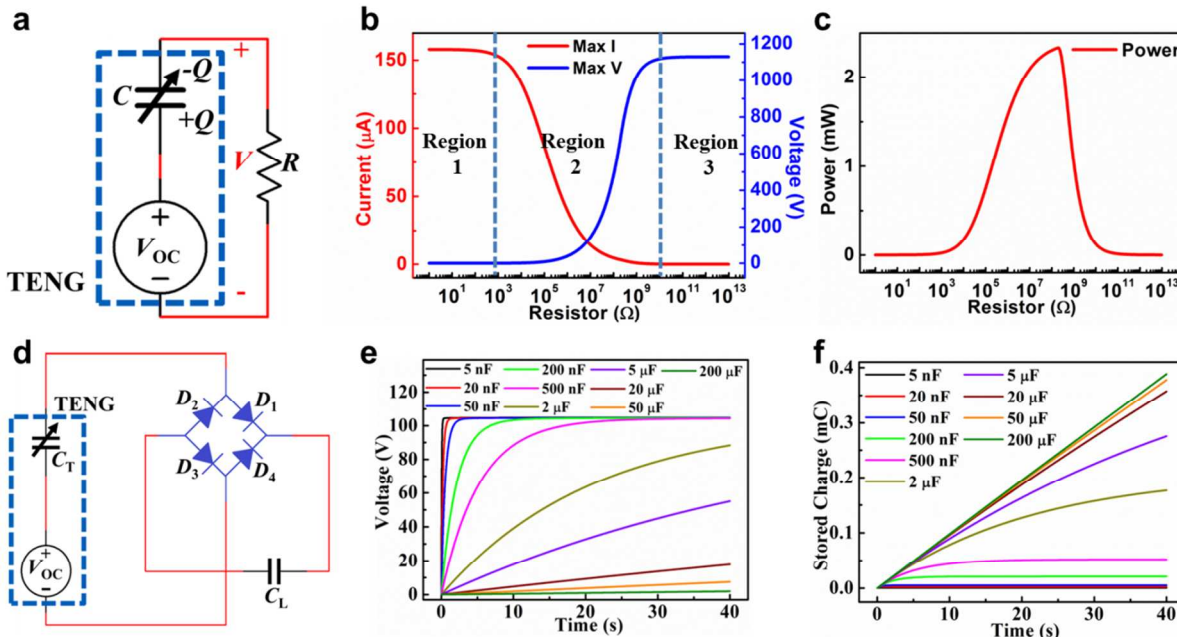


**Fig. 5** Theoretical investigations on the energy harvesting system based on TENGs.<sup>89,90</sup> (a) The equivalent circuit of the TENG based energy harvesting system for its resistive load characterization. (b) The numerically calculated peak values of the voltage and current on different loads when the TENG is under a uniform velocity separation. (c) The influence of the load resistance on the instantaneous power output. (d) The circuit diagram design for the TENG charging characterization under periodic mechanical motion. (e) Voltage-time relationship at different load capacitances. (f) Stored charge-time relationship at different load capacitances.

The other case is the TENG's charging characteristics under periodic mechanical motion. As shown in Fig. 5d, it is a circuit diagram design for the TENG charging system. As demonstrated in Fig. 5e, a saturation charging curve is observed for all the load capacitors. At the beginning, the load capacitor is charging at a maximum speed. Then, the charging speed gradually slows down and finally saturates at the same value. Furthermore, the stored charge-time relationship at different load capacitances was also studied. As shown in Fig. 5f, at beginning, the curves for all load capacitors converge to a linear curve. As time increases, the curves shift downwards first and finally get saturated. Till this point, very few charges can be charged into the capacitor. Both the resistive output and charging characteristics are critically important for the optimized design for energy harvesting system based on TENGs.

## 4. TENG as a sustainable power source

### 4.1 Enhancement of instantaneous output power through advanced structural design

Continuously seeking new methodology for enhancing the TENG's output is always a goal. Enabled by an advanced structural design of two radial-arrayed fine electrodes that are complementary on the same plane, the planar-structured TENG generates periodically changing triboelectric potential that induces alternating currents between electrodes.<sup>47</sup> The TENG has a multi-layered structure, which consists of mainly two parts, i.e., a rotator and a stator, as sketched in Fig. 6a. A photograph of an as-fabricated device is demonstrated in Fig. 6b. For quantitative characterization, a programmable rotary motor was connected to the rotator that was in co-axial alignment with the stator. At a rotating rate of 500 r min<sup>-1</sup>, the short-circuit current ( $I_{sc}$ ) has a continuous AC output with an average amplitude of 0.5 mA and a frequency of 500 Hz (Fig. 6c). For open-circuit voltage ( $V_{oc}$ ), it oscillates at the same frequency with a peak-to-peak value of 870 V (Fig. 6d). Furthermore, it is found that the matched load is also a variable value, exhibiting a reversely proportional relationship with the rotation rate, as shown in Fig. 6e. Consequently, linearly rising output power can be obtained at higher rotation rates.

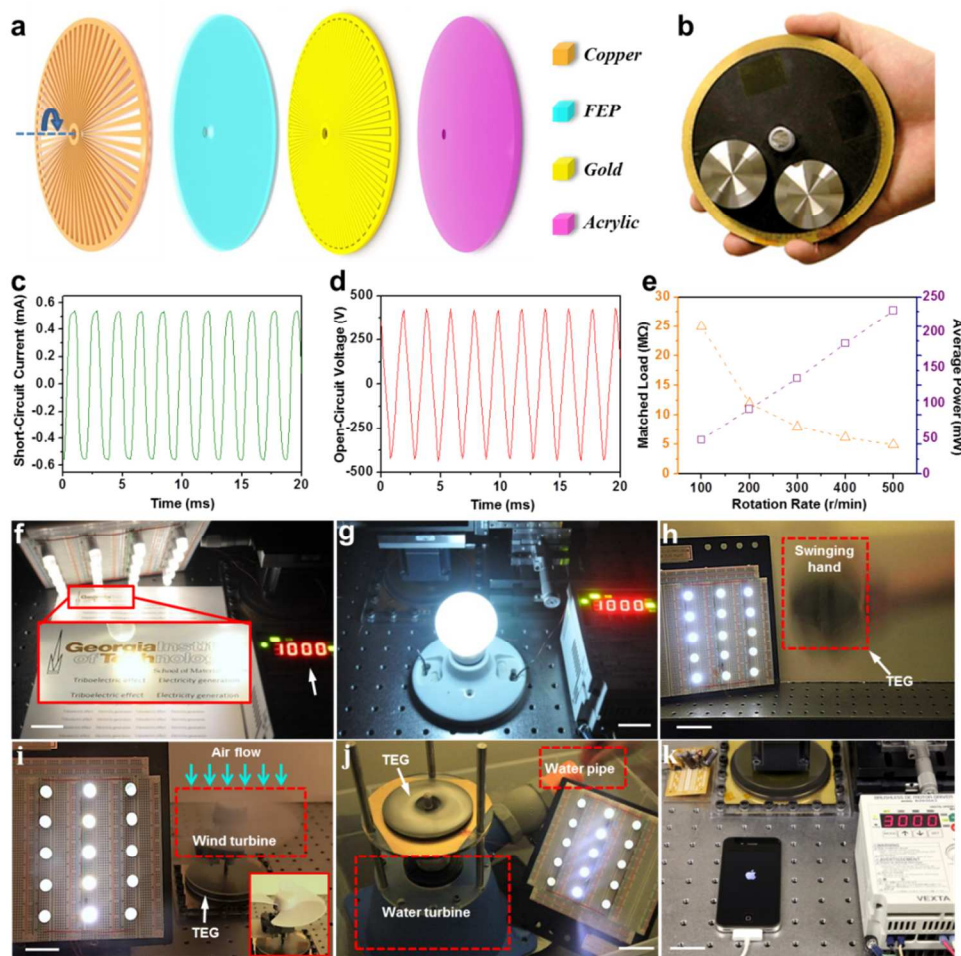


**Fig. 6** Radial arrayed triboelectric generator for high-performance mechanical energy harvesting.<sup>47</sup> (a) Schematic illustrations of the triboelectric generator, which has two parts, that is, a rotator and a stator. (b) A photograph of an as-fabricated triboelectric generator. The short-circuit current (c) and open-circuit voltage (d) of the triboelectric generator under a rotation rate of 500 r/min. (e) Matched load resistance and average output power with increasing rotation rate. (f) Photograph of the reading illumination by the 20 spot lights in complete darkness with the triboelectric generator as a direct power under a rotation rate of 1000 r/min. (g) Photograph of a G16 globe light that is directly powered by the triboelectric generator under a rotation rate of 1000 r/min. Photograph showing that the triboelectric generator harvested energy from human hand swinging (h), air flow (i) and water flow (j). And about 15 spot lights were lighted up simultaneously. (k) Photograph of a cellphone that is being charged by the power-supplying system, which consists a triboelectric generator and a power management circuit. All the scale bars are 3 cm. Reproduced with permission from Nature Publishing Group.

And the TENG can deliver an optimum average output power of  $\sim 1.5$  W at the matched load of  $\sim 0.8$  M $\Omega$  under a rotation rate of 3000 r min<sup>-1</sup>, which corresponds to an average output power density of 19 mW cm<sup>-2</sup>. To demonstrate the capability of the TENG as a direct power source, regular light bulbs were electrically connected as indicators. Under the rotation rate of 1000 r min<sup>-1</sup>, a total of 20 spot lights were simultaneously lighted up, providing sufficient illumination even for reading printed text in complete darkness (Fig. 6f). And the generated power can also light up a white globe light

(Fig. 6g). Furthermore, the TENG can also be applied to harvest energy from ambient environment. Firstly, the TENG can harvest mechanical energy from body movement. As illustrated in Fig. 6h, the compact-sized TENG in a hand had pieces of inertia mass fixed on the rotator. As the hand swung back and forth in small amplitude, the generated power from the relative sliding friction between the rotator and stator can light up 15 spot lights simultaneously. Then the TENG was demonstrated to harvest energy from light air flow at a flow speed of 6 m/s, and still 15 spot lights was lighted up

simultaneously (Fig. 6i). In addition, the TENG is capable of harvesting energy from water flow. At a flow rate of 5.5 L/min, the generated electricity can also light up 15 spot lights simultaneously. In addition, a power supplying system was further established, which consists of a TENG and a power management circuit. And it can deliver a DC output at a constant voltage of 5 V in less than 0.5 sec

after the TENG starts to operate. As shown in Fig. 6k, the power supplying system is able to serve as a charging source for batteries. Since 5 V is the standard charging voltage for most of the commercial portable electronics, a cellphone automatically turned on once the voltage output shot to 5 V due to the operation of the TENG.

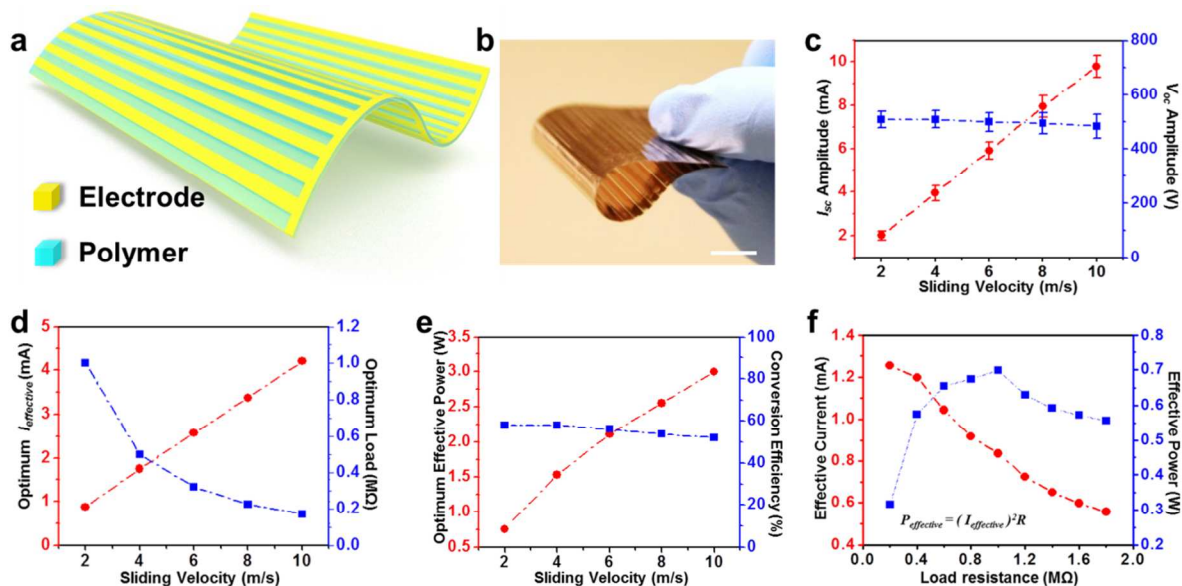


**Fig.7** A thin-film-based micro-grating triboelectric nanogenerator (MG-TENG) for high-performance mechanical energy harvesting.<sup>20</sup> Schematic illustration (a) and a photograph (b) of the MG-TENG. (c) The sliding velocity depended current and voltage output of the MG-TENG. (d) The optimum effective current and corresponding load with varying sliding velocity. (e) The optimum effective power of the MG-TENG with varying sliding velocity. (f) Load matching test at a sliding velocity of 2 m/s. Maximum effective power is obtained at the matched load of 1 MΩ. Reproduced with permission from Wiley.

Furthermore, a thin-film-based micro-grating triboelectric nanogenerator (MG-TENG) is also developed for high-efficiency power generation through conversion of mechanical energy.<sup>20</sup> The shape-adaptive MG-TENG relies on sliding electrification between complementary micro-sized arrays of linear grating, which offers a unique and straightforward solution in harnessing energy from relative sliding motion between surfaces. Fig. 7a is a schematic illustration of the MG-TENG, while Fig. 7b is a photograph of the as-fabricated device, which is extremely thin and flexible. The scale bar is 1 cm. And the sliding velocity depended electric output of the MG-TENG is characterized. As shown in Fig. 7c, a nearly linear relationship between the amplitude of short-circuit current ( $I_{sc}$ ) and the sliding velocity can be obtained. While, the open-circuit voltage ( $V_{oc}$ ) is independent of the sliding velocity. In the meanwhile, as shown in Fig. 7d, the corresponding matched load is approximately

reversely proportional to the sliding velocity. Thus, the optimum effective current is also linearly related to the sliding velocity, as demonstrated in Fig. 7e. To evaluate the capability of the MG-TENG for power generation, resistors were utilized as external loads for characterization. As displayed in Fig. 7f, the current amplitude drops with increasing load resistance owing to the ohmic loss, and the effective power is maximized to a value of 0.76 W at a load resistance of 1 MΩ and a sliding velocity of 2 m/s. And operating at a sliding velocity of 10 m/s, an MG-TENG of 60 cm<sup>2</sup> in overall area can deliver an average output power of 3 W and a power density of 50 mWcm<sup>-2</sup> at an overall conversion efficiency of 50%. Holding a collection of compelling features, including high electric output power, extremely light-weight, low cost, scalability and adaptability, the MG-TENG is another practically effective approach in

harvesting ambient mechanical motions as well as possibly producing electricity at a large scale.

#### 4.2 Enhancement of energy conversion efficiency

Various efforts have been committed to improve the energy conversion efficiency of TENG. In this regard, a linear grating-structured freestanding triboelectric-layer nanogenerator (GF-TENG) was demonstrated.<sup>22</sup>

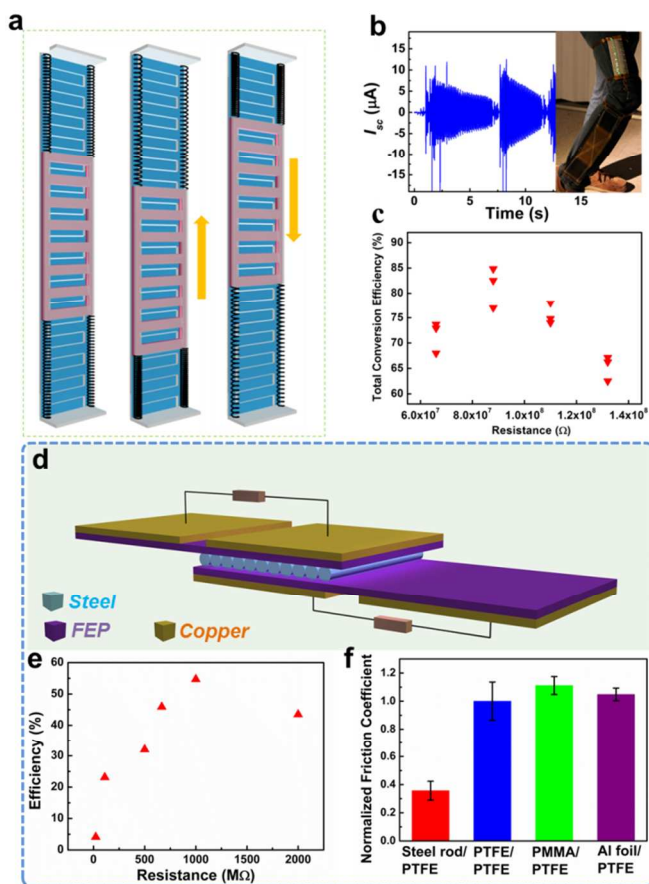


**Fig. 8** A linear grating-structured freestanding tribo-electric-layer nanogenerator (GF-TENG) for high-efficiency mechanical energy harvesting.<sup>22</sup> (a) Schematic illustration of the device structure for non-contact GF-TENG. (b) The real-time measurement of the short-circuit current when people walking with non-contact GF-TENG. (c) Total conversion efficiency of the device for harvesting slight vibration under different load resistances. (d) Schematic illustration of the device structure of the rolling triboelectric nanogenerator.<sup>78</sup> (e) Calculated energy conversion efficiency with various load resistances. (f) Normalized friction coefficient between different types of materials customized for triboelectric nanogenerators. Reproduced with permission from American Chemical Society and Wiley.

The device mainly consists of two groups of components: a freestanding triboelectric layer with grating segments and two interdigitated metal electrodes. And triboelectric layer was suspended and anchored by four soft springs, as illustrated in Fig. 8a. Due to the unique structural design, the GF-TENG excels in low-frequency vibration energy harvesting with superior energy conversion efficiency. As shown in Fig. 8b, the GF-TENG is anchored on a human leg, and the corresponding real-time short-circuit current is measured. Each walking step produced many cycles of residual vibrations of the segment around the equilibrium position, and electricity was generated in each cycle of the free vibration although the mechanical triggering from the leg was stopped. Fig. 8c shows the estimated total conversion efficiency under different external resistances from a number of repeated measurements. At a matched external resistance of  $88 \text{ M}\Omega$ , a total energy conversion efficiency of 85% has been obtained. Here, the energy conversion efficiency accounts all of the electricity generated by the residual vibrations of the device.

In comparison to sliding mode electrification, rolling electrification may consume less mechanical energy without scarifying the electric output, which renders itself a highly efficient approach for mechanical energy harvesting. The device structure of a rolling triboelectric nanogenerator (RTENG) is schematically illustrated in Fig. 8d, which is composed of a group of rolling steel rods sandwiched by two layers of FEP thin films.<sup>78</sup> And copper was coated onto the FEP film as back electrodes. Fig. 8e shows the load resistance dependent energy conversion efficiency, which indicates that the instantaneous efficiency can be up to 55% at an optimized external resistance. The high energy conversion efficiency can be attributed to the low frictional coefficient between the rolling rods and the planar FEP surface, which is verified by the measurement of the normalized friction coefficient (Fig. 8f). It can be found that the rolling rod structure holds a substantially lower frictional coefficient than that of the planar structures.

#### 4.3 Optimization of surface charge density

Surface charge density is essentially correlated to the output performance of the TENG. Manipulating the surface charge density can potentially be utilized to enhance the output performance of energy harvesting devices or nullify contact electric charge transfer. Different approaches have been taken to modulate the surface charge density. The surface charge density can be measured by an atomic force microscope (AFM).<sup>91</sup> The AFM tip was Pt coated and scanned

over a Parylene surface with a bias. The surface charge density is then characterized by the scanning Kelvin potential microscopy (SKPM). An energy band diagram for the metal and dielectric materials in the situations of pre-contact was presented in Fig. 9a. When the bias is more positive than the nullified bias, electrons will flow from the dielectric to the metal, leaving the dielectric surface

positively charged. In the meanwhile, a negative bias to the metal can raise the Fermi energy level, driving more electrons flow to the dielectric surface to fill up the higher surface energy states, which will lead to a more negatively charged dielectric surface compared with that of without applied electric field.

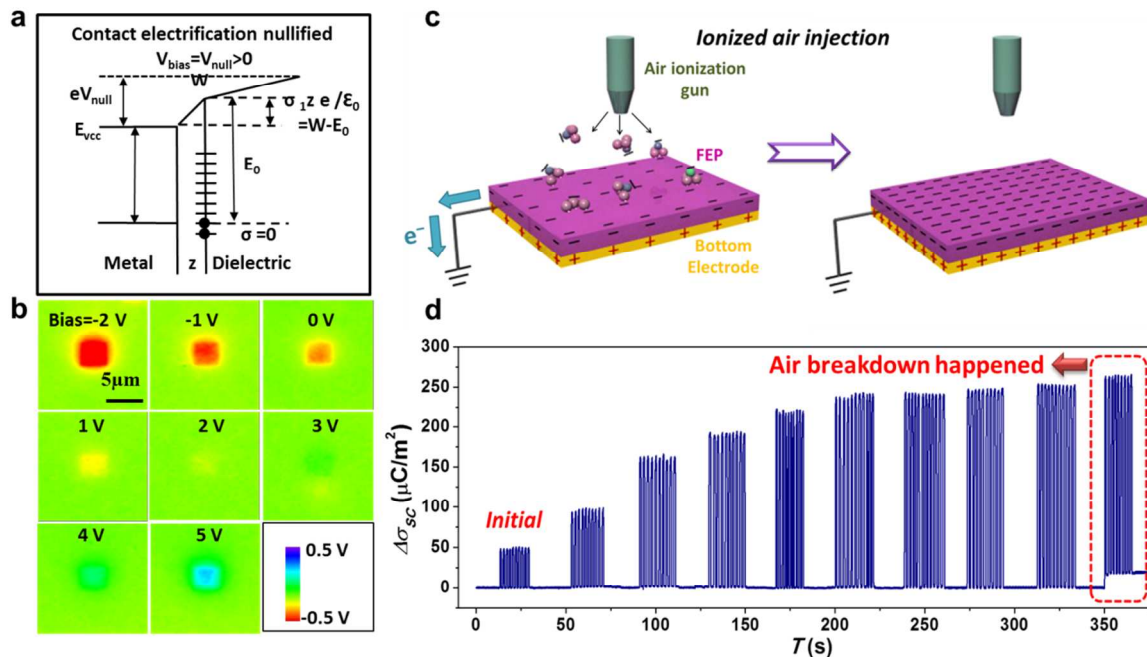


**Fig. 9** Optimization of the surface charge density for an improved triboelectric nanogenerator output performance. (a) An energy band diagram for the metal and dielectric materials in the situations of precontact. (b) The surface potential distribution in the AFM tip rubbed areas. (c) Schematic illustration showing a basic process of the ion injection on the FEP film. (d) Short-circuit charge density generated by the TENG when the FEP film was injected with ions time-by-time. Reproduced with permission from American Chemical Society<sup>91</sup> and Wiley.<sup>92</sup>

To quantify the relationship between the applied electric field and the surface charge density, fresh areas of a Parylene film with a thickness of 2  $\mu\text{m}$  were rubbed under various applied biases from -10 to 10 V. And the surface potential distribution in the areas was shown in Fig. 9b. And the measurement was performed under a bias from -2 to 5 V. The results indicate that a negative bias can enhance the negative charge density, a positive bias of 2 V can almost nullify the charges and a bias of higher than 2 V can bring positive charges to the rubbed surfaces. The study demonstrates an effective approach for surface charge density manipulation.

The surface charge density can be enhanced by ionized-air injection. *Via* adjusting the injection cycles, the surface charge density can be directly controlled to possibly reach a higher level.<sup>92</sup> A basic process of the ion injection on the FEP film is demonstrated in Fig. 9c. And the negative ions were injected onto the FEP surface

from an air-ionization gun. The back electrode of the FEP film is grounded during this process so that the positive charges can be induced onto the electrode to screen the electric field from the injected negative charges. After the ion injection, the FEP surface and its back electrode holds the opposite charges with the same density. Fig. 9d shows the short-circuit charge density generated by the TENG when the FEP film was injected with ions time-by-time. At an initial stage, the TENG only produced triboelectric surface charge density on the FEP surface due to the contact electrification. Subsequently, the ion injection led to the elevation of the surface charge density step by step, which can contribute to an increased output performance. And Wang *et al.* also demonstrated a prior-charge injection process to enhance the surface charge density.<sup>93</sup> In addition, to functionalize the contact surface, for example, the polyethylene terephthalate (PET) films either with

poly-L-lysine solution or trichloro (1H,1H,2H,2H-perfluorooctyl) silane (FOTS) can also enhance the surface charge density, which would lead to high performance triboelectric nanogenerators.<sup>94</sup> Still, Jeong *et al.* developed a highly functional and controllable nanostructures *via* block copolymer self-assembly to modulate the contact-surface area and the frictional force for an enhanced triboelectrification.<sup>95</sup>

#### 4.4 Enhancement of output current based on multi-layer integrations

The application of TENG for mechanical energy harvesting may be challenged by its low output current, and a possible solution is to synchronize the outputs of all multiple units so that the instantaneous output power can be maximized.

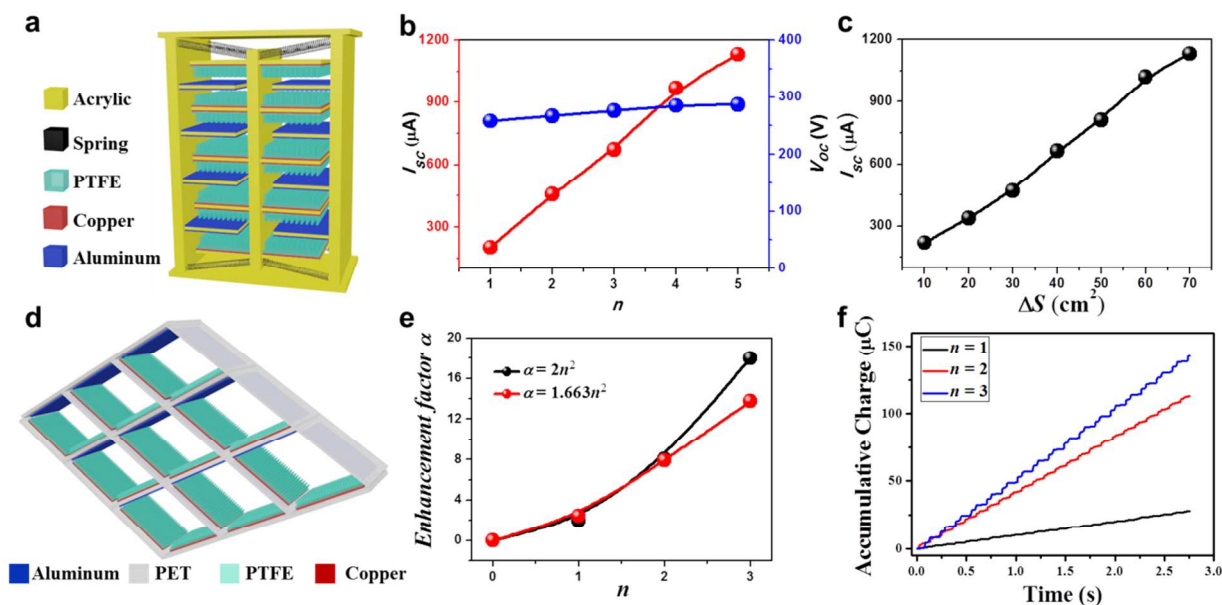


**Fig. 10** Enhancement of the output current of TENG based on multi-layer integrations. (a) Schematic illustration of the multi-layered stacked TENG.<sup>96</sup> (b) Dependence of electric output on the number of pinned fingers  $n$ . (c) Dependence of the short-circuit current on effective contact area ( $\Delta S$ ) of the TENG with  $n = 5$ . (d) Sketch of an integrated rhombic gridding based triboelectric nanogenerator.<sup>36</sup> (e) The current's enhancement factor  $\alpha$  is increasing as a function of number of unit cells along the edge length  $n$ . (f) Accumulative inductive charges generated by the TENG with  $n = 1, 2$  and  $3$ , respectively. Reproduced with permission from Wiley and American Chemical Society.

In this regard, a multi-layered stacked TENG was developed as a cost-effective, simple and robust approach for harvesting ambient mechanical energy.<sup>96</sup> The 3D-TENG has a multilayered structure with acrylic as supporting substrates, as schematically shown in Fig. 10a. Acrylic was selected as the structural material due to its decent strength, light weight, good machinability and low cost. And the total number of the units in a 3D-TENG can be expressed as:

$$N = 4n \quad (5)$$

where  $n$  is the number of pinned fingers of a TENG. Eight identical springs were employed to bridge the moveable and pinned fingers.

As shown in Fig. 10b, the voltage output is almost constant for 3D-TENGs with  $n = 1 \sim 5$ , which is attributed to the electrically parallel connection among all of the units. However, the current output is a monotonically increasing function of  $n$ . Such a dramatic current enhancement is mainly owing to the operating synchronicity

of all units. In the meanwhile, a monotonically increasing relationship was also observed between the current output and the effective contact area  $\Delta S$ , as shown in Fig. 10c. The experimental observation convincingly demonstrates the effectiveness of 3D-TENG for current output enhancement.

To enhance the output current for the TENG based mechanical energy harvesting, here, we also demonstrated another rationally designed device with integrated rhombic gridding, which can also greatly improve the total current output owing to the multiple unit cells connected in parallel.<sup>36</sup> The structure of integrated rhombic gridding based TENG is shown in Fig. 10d, in which, the total number of unit cells in one TENG can be expressed as:

$$N_{total} = 2n^2 \quad (6)$$

where  $n$  is the number of unit cells along the edge length. Each polyethylene terephthalate (PET) sheet with a thickness of 600  $\mu\text{m}$  is

cut half through and then lock into each other to form the framework of TENG. In each unit cell, aluminum thin film with nanoporous modification plays dual roles as a contact electrode and a contact surface and PTFE with back coated copper plays as another contact surface.

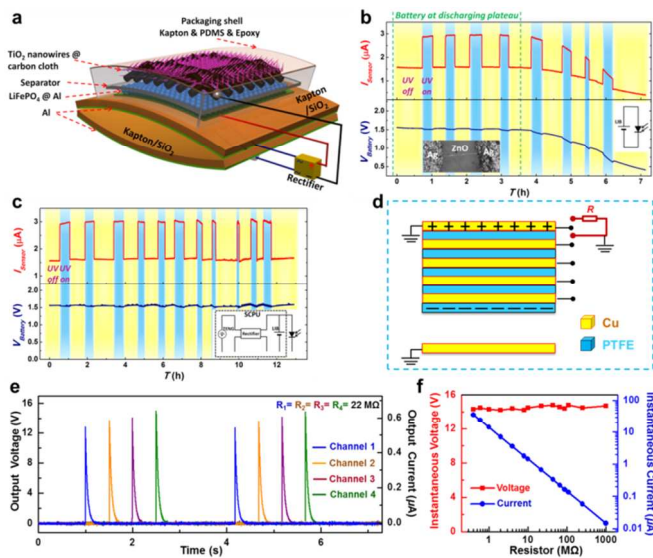


**Fig.11** Energy storage and power management of TENGs. (a) Schematic diagram of the structural design of the self-charging power unit.<sup>99</sup> (b) Operation of the UV sensor when solely driven by the LIB part in the SCPU. (c) The operation of the UV sensor continuously driven by the SCPU for  $\sim 13$  h. (d) Sketch of a multilayered-electrodes-based TENG (ME-TENG).<sup>101</sup> (e) The output voltage and current curves of the four-channel ME-TENG with an identical channel load resistance of 22 MΩ. (f) The resistance-dependent properties of the four channels ME-TENG. Reproduced with permission from American Chemical Society and Wiley.

As indicated in Fig. 10e, the current enhancement factor  $\alpha$  is a function of the number of unit cells along the edge length,  $\alpha = bn^2$ . The fitting result renders the coefficient  $b$  a value of 1.66. Considering the non-ideal experimental factors, such as humidity, particle contaminations in air, and other experimental imperfection, the observed result of enhancement factor is considerably approaching to the ideal value of  $2n^2$ , revealing that the effectiveness of the integrated rhombic gridding structure for current enhancement. As illustrated in Fig. 10f, the accumulative induced charges also increases with  $n$ , which reaches up to 142.68  $\mu\text{C}$  within 2.75 s when  $n = 3$ , further indicating that the integrated rhombic gridding structure can dramatically enhance the electric output of TENG. In

addition, Tang *et al.* also demonstrated a stacked triboelectric nanogenerator to enhance the electric output. By employing a 3-layer-stacked structure, the device with an area of 1.5 cm  $\times$  2.5 cm can produce an open-circuit voltage of 430 V and a short-circuit current of 12  $\mu\text{A}$ . Meng *et al.* also presented a self-powered flexible printed circuit (FPC) board with an integrated zigzag-shaped TENG. And it was demonstrated that, with 10 integrated friction pairs, the devices produced a voltage of about 620 V with a current density of 45.1  $\mu\text{A}/\text{cm}^2$ . In addition, a three-dimensional multi-layered sliding TENG was also demonstrated.<sup>97</sup> With 20 layers, the current density was up to 5.5 mA  $\text{m}^{-2}$ . And Tang *et al.* also developed a cylindrical TENG by segmentation design and multilayer integration, and the output power was also greatly enhanced.<sup>98</sup>

#### 4.5 Energy storage and power management of TENGs

The output of the TENGs usually contains noncontinuous pulses with irregular magnitude. As a result, it is hard to be directly used for driving electronic devices that need a constant DC voltage. Energy storage, such as battery, could be a solution to this problem. On one hand, the batteries can provide a constant voltage at the discharging plateau to act as the direct power sources for most portable electronics. On the other hand, an essential problem with battery is its limited lifetime, while the TENG can act as a sustainable power source to the batteries. Thus, to develop a sustainable power source with constant voltage output, a flexible self-charging power unit (SCPU) is developed.<sup>99</sup>

Figure 11a is the schematic diagram of the structural design of the SCPU, which is an integration of a flexible Li-ion battery and an arch-shaped TENG structure. To prove the SCPU as a sustainable power source for small electronic systems, a ZnO-nanowire-based UV sensor was fabricated for demonstration, as the left inset of Fig. 11b shows. As a comparison, we used a fully charged Li-ion battery portion of the SCPU to power the UV sensor. After about 3.5 h, the voltage started to drop due to the running out of the charge of the battery, as shown in Fig. 11b. After 4 hours' usage, the current level for the UV-off and UV-on states both decreased to a low level, indicating that the battery has to be replaced. The limited lifetime problem can be well solved if using the SCPC as a power source. Resort to a hybridization of the mechanical energy harvesting and energy storage in the SCPU, the UV-sensor can be truly self-powered continuously and sustainably. As demonstrated in Fig. 11c, there is no observable drop of the current and voltage output even powering the electronic system for continuously 13 hours. In

addition, very recently, another self-charging power unit was also reported. It consisted of a textile TENG and a flexible lithium-ion battery, which could act as sustainable power sources for wearable electronics.<sup>100</sup>

On the other hand, the relatively high voltage output and low current output great hinders the TENG for practical applications. A transformer could provide a solution, but it has a high working frequency and low-input load resistance, which does not match with the low-frequency and high-output load resistance characteristics of the TENG. To lower the output voltage while preserving the total power, a multilayered-electrodes-based TENG (ME-TENG) is demonstrated, as sketched in Fig. 11d, which is designed by allowing the current to flow multiple times as controlled by a mechanical switch during the sliding of the TENG.<sup>101</sup> Under an identical channel load resistance of 22 M $\Omega$ , the output voltage and current curves of the four-channel ME-TENG is presented in Fig. 11e. Four peaks with similar peak heights and widths appear in sequence, which respectively correspond to the pulsed output signals in the four channels. Still a further step was taken to study the resistance-dependent properties of the four channels ME-TENG, as the results shown in Fig. 11f. The measured instantaneous voltage holds constant around 14.3 V in a wide range from 0.4 M $\Omega$  to 1 G $\Omega$ . However, the measured instantaneous current and power renders a linear relationship with 1/R. And the current decreased from 35.8  $\mu$ A to 14.7 nA with the power from 0.51 mW to 0.22  $\mu$ W when the resistance varying from 0.4 M $\Omega$  to 1 G $\Omega$ . In a word, the ME-TENG reported an approach to manage the output voltage by controlling the charge flow in a process of multiple steps, which results in the lowering of the voltage and the increasing of total charge transport.

## 5. Hybridization of triboelectric nanogenerators with other types of energy harvesters

As the operation environment of mobile electronics varies, the energy that may be available may be light, mechanical, thermal and even chemical. An iWatch is a typical example advantageous to integrate other types of energy harvesters for simultaneously scavenging energy from various sources, which is referred to as a hybrid cell first introduced in 2009.<sup>102,103</sup> The hybrid cell usually consists of a TENG and another type of power generator, such as solar cell,<sup>104-106</sup> electromagnetic generator,<sup>107,108</sup> thermoelectric generator,<sup>109</sup> electrochemical cell,<sup>110</sup> etc. Based on different output profiles, the hybrid cells can be classified into AC-AC hybrid cell

and AC-DC hybrid cell. On the other hand, the TENGs can also be integrated with energy storage units, like lithium ion batteries or supercapacitors, to realize the self-powered operations of electronic devices and systems. The self-powered system has a lot of potential applications in portable electronics, sensor networks, internet of things, implanted devices, and in-vivo biomedical monitoring.

### 5.1 TENG-based AC-AC hybrid cell

Besides the TENGs, many other types of mechanical energy harvesting approaches have been developed, including the piezoelectric generators, the electromagnetic generators, and the electrostatic generators. Each of them has their unique advantages and drawbacks, while the output profiles are all alternating manner. Hence, by integrating TENGs with one of the above-mentioned generators, the hybrid cell is enabled to take advantages of both of their unique characteristics. For instance, the electromagnetic generator requires much lower optimum resistance, and the output current is also much higher, while its output voltage is lower than that of the TENG.

Zhang *et al.* demonstrated a hybrid cell composed of TENG and electromagnetic induction generator (EMIG), as shown in Fig. 12.<sup>111</sup> First, the theoretical governing equations for both the TENG and EMIG were compared, and their structural and output similarities were revealed. Moreover, the output performances of both the TENG and EMIG for harvesting mechanical energies from both reciprocating and rotating motions were presented. It was then concluded that the EMIG could serve as a voltage source with low internal impedance TENG worked as a current source with much higher internal impedance. For integration of the two power generators, the generated output could be rectified and connected both in series and in parallel. In parallel connection, the hybrid cell behaves like an ideal voltage source, with a low optimum resistance of 12.3  $\Omega$ . While in series connection, the hybrid cell behaves like an ideal current source, with a high optimum resistance of 13.8 M $\Omega$ . In both cases, the optimum output power was only close to that of the EMIG in parallel connection or the TENG in series connection, and almost half of the power output was lost through the coupling of the two power generators because of the mismatch of internal impedances.

To solve this compatibility problem, the rectified EMIG was connected with a resistor in series connection and the rectified TENG was connected with a resistor in parallel connection. With this power transforming approach, the optimum resistances of both

generators were brought much closer to 9.43-9.77 k $\Omega$ , with their output power density of 117.6-118.1 nW.

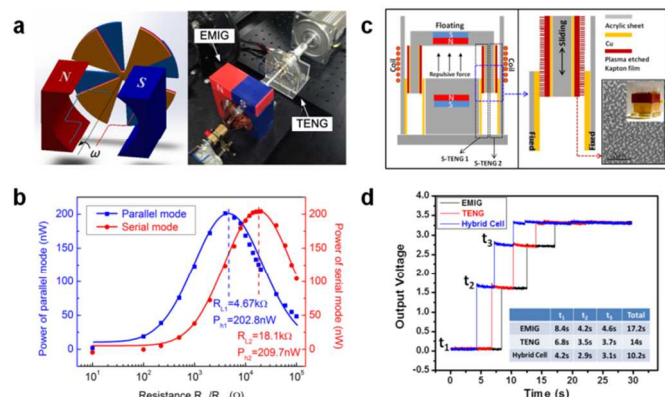


**Fig. 12** The hybrid cell composed of EMIG and TENG. (a) A schematic diagram and photograph of the hybrid rotating EMIG and TENG, and their conjunction operations.<sup>111</sup> (b) The relationship between the output power and the resistance of the external load in both parallel and serial modes. (c) Left: a cross section view of the hybrid cell. The two dashed black boxes indicate the locations of two S-TENGs. Right: an enlarged view of the S-TENG structure circled by the purple dashed box. The inset is the SEM image taken on the Kapton film's surface with nanowire structures and a photo of the real device.<sup>107</sup> (d) Voltage curves showing the charging process of a commercial buck converter board by the EMIG, TENG, and hybrid cell to convert the ac signal into a regulated dc voltage. There are three steps. The inset table lists the time used for each step in three cases. Reproduced with permission from Wiley and American Chemical Society.

For a conjunction operation of the EMIG and TENG, the two rotary generators shared the same shaft, and connected with an external resistor in series and parallel, respectively (Fig. 12a). Then, the two transformed generators could be connected in both parallel mode and series mode, and their integrated output powers were displayed in Fig. 12b. The maximum power of 202.8 nW was delivered with an optimized external resistance of 4.67 k $\Omega$  for the two power sources in parallel connection, while the maximum power of 209.7 nW was obtained with an optimized external resistance of 18.1 k $\Omega$  for the two power sources in serial connection. Both values were close to the theoretical value of 235.2 nW, confirming the high efficiency of this conjunction approach. Fan *et al.* also did a comparison between the EMIG and TENG, and it also found that the power output performances of the EMIG and the TENG have a special complementary relationship, with the EMG being a voltage source and the TEG a current source.<sup>112</sup> Alternatively, Hu *et al.*

demonstrated another approach to hybridize the TENG and the EMIG in a more compact approach,<sup>107</sup> as shown in Fig. 12c. The basic device structure is composed of a smaller hollow cube with an opening bottom floating on top of a solid stand with a larger hollow cube surrounding it. The side wall surfaces of the solid stand and the larger hollow cube are covered with copper foil, and copper-coated Kapton thin films are attached on both the inner and outer surfaces of the smaller hollow cube. The floating of the smaller hollow cube is maintained by the balance between its gravity and the repulsive force between two magnets embedded in the solid stand and the smaller hollow cube, respectively. The two contact surfaces between Kapton films and copper foils construct two sliding-mode TENGs (S-TENGs), as indicated by the right inset of Fig. 12c. Then, a copper wire is wrapped around the outer surface of the larger hollow cube with 300 turns. As the floating magnet is oscillating with an external force, the magnetic flux in the coil will be altered, and an output current will be produced in the coil due to electromagnetic induction. The output performances of both the TENG and the EMIG were recorded. The EMIG generates a high short-circuit current of up to 12.5 mA, but a low open-circuit voltage of 1.5 V. On the contrary, the open-circuit voltage of the TENG can reach around 500 V with an integrated short-circuit current of 30  $\mu\text{A}$  at the sliding mode or 400  $\mu\text{A}$  at the contact mode. In terms of frequency dependence of the output performance, the  $V_{OC}$  of the TENG keeps constant with increasing frequencies, while its  $I_{SC}$  increases with the frequency of motions. On the other hand, both the  $V_{OC}$  and the  $I_{SC}$  of the EMIG increase drastically with the frequency, indicating the distinct working principles between the EMIG and the TENG. The optimum output powers of the TENG and the EMIG are 22.5 mW and 5.8 mW, respectively, with the matching resistance of 10 M $\Omega$  and 90  $\Omega$ . To obtain impedance match between the two contributing power generators, power transformers were connected with the TENG and EMIG to adjust their optimized external resistance to around 5 k $\Omega$  with the maximum output power of 7.7 and 1.9 mW. The loss of power is mainly attributed to the inconsistency of working frequency between the power generators (12 Hz) and the transformers (60 Hz), which can be greatly improved by adjusting the working frequency or the type of transformers.

A major advantage of this new hybrid cell is that due to the rational design, the output signals from both the TENG and EMIG are in phase. Thus, they can be added constructively and directly. Another important characteristic of the device after impedance match is that the output voltages from both the TENG and EMIG are

adjusted to a similar level, around 4.6 V with a matched load of 5 k $\Omega$ . The output current in the EMIG and TENG in this case is about 0.4 and 1.6 mA, respectively. When these two parts were connected in parallel, the output voltage was maintained, and the output current increased to 2.2 mA, which is a little larger than the sum of the output currents from the EMIG and TENG. The hybrid output power was then regulated through a commercial power management circuit board (LTC3588-1, Linear Technology). The AC signals were rectified by the full-wave bridge, and the generated charges were stored in the capacitors, by which a regulated output voltage of 3.3 V was achieved in a three-step process, as shown in Fig. 12d. It can be found that the time required to charge the board for the hybrid cell is less than that for each of the individual generator. With the regulated output power and the constant output voltage, the hybrid cell was enabled to drive a half-adder circuit, which demonstrated an important application of the hybrid cell in self-powered computation and processors.

Besides the above works that employ the hybridization of triboelectrification and electromagnetic induction, a few more efforts were also conveyed to develop other types of hybrid cell with two power generators with AC output characteristics. For instance, Yang *et al.* fabricated a hybrid cell based on the triboelectric effect between PET and PDMS, and the pyroelectric effect of a PZT thin film.<sup>113</sup> Hence, this hybrid cell can be utilized to simultaneously harvest mechanical and thermal energies. The hybrid output power was rectified and stored in a lithium ion battery, and self-powered degradation methyl orange was realized by the hybrid energy cell, due to the generation of super-oxidative hydroxyl radical on the anode. This research opens up potential applications in waste water treatment. Moreover, Zi *et al.* continued to develop a new technology to scavenge the heat flow energy caused by the friction motion of a sliding TENG.<sup>114</sup> In this work, a triboelectric-pyroelectric-piezoelectric hybrid cell was fabricated with PTFE and PVDF thin films to effectively harvest the reciprocating mechanical energy. First, the sliding TENG worked based on the sliding motion between the Al and the PTFE thin films. Then, the pyroelectric and piezoelectric effects of the underlying PVDF thin film was employed for harvesting the friction-induced heat energy and the mechanical energy from the variation of the normal force, respectively. This hybrid cell has been demonstrated to extend the illumination time of a LED and to quickly charge a capacitor. Furthermore, it can also be applied as a self-powered temperature and force sensor during the friction motion. Bai *et al.*

also demonstrated the output power enhancement of TENG by coupling of contact electrification and the piezoelectric effect of PVDF thin film.<sup>115</sup> In this work, the triboelectric charge density was significantly improved due to the piezoelectric polarization in the forward direction. The  $J_{SC}$  was improved by 36.3% as compared to the non-polarized TENG, while a decrease of output was observed for the reversely polarized counterpart, and the improvement mechanism was verified. Similarly, Han *et al.* also developed a r-shaped hybrid nanogenerator by use of the piezoelectric effect of PVDF and the triboelectric effect between the aluminum and PDMS.<sup>116</sup> Through one cycle of electric generation of the hybrid cell, 10 light-emitting diodes are lighted up instantaneously, and a 4-bit liquid crystal display can display continuously for more than 15 s. The hybridization between the piezoelectric and triboelectric effect was also demonstrated by a 3D fiber-based nanogenerator, which is composed of one coaxial carbon fiber and one nylon fiber.<sup>117</sup> ZnO nanorods were grown the carbon fiber and deposited with Cu electrode on top. A layer of PDMS thin film deposited with Cu electrode was wrapped around this composite structure with an insulating Nylon film. In the operation of the hybrid nanogenerator, the Nylon fiber get contacted with the PDMS layer and pressed on the carbon-fiber-based composite structure. Hence, piezoelectric output can be measured from the conducting carbon fiber and the copper electrode on top of the ZnO nanorod array; and triboelectric output can be generated between the copper electrode on the PDMS layer and the ground. This hybrid nanogenerator can be further applied as a self-powered pressure sensor for anti-theft detections.

## 5.2 TENG-based AC-DC hybrid cell

As compared to the AC-AC hybrid cell, the other type of hybrid cell usually consists of a TENG for harvesting mechanical energy, and another nanogenerator for harvesting other type of energy sources, like thermal, chemical, and solar energies. In this regard, the other component of the hybrid cell may display distinct output characteristics and performances. First, most of these power generators have high output current but low output voltage; Second, the internal impedance of these energy cells are usually much lower than that of the TENG; Third, the output profile of these energy cells are usually constant DC signals rather than oscillating AC signals. These output characteristics are significantly different from the TENGs and can be employed as important supplementary adding up to the TENGs, though challenges still exist in the integration and compatibility between the two types of generators.

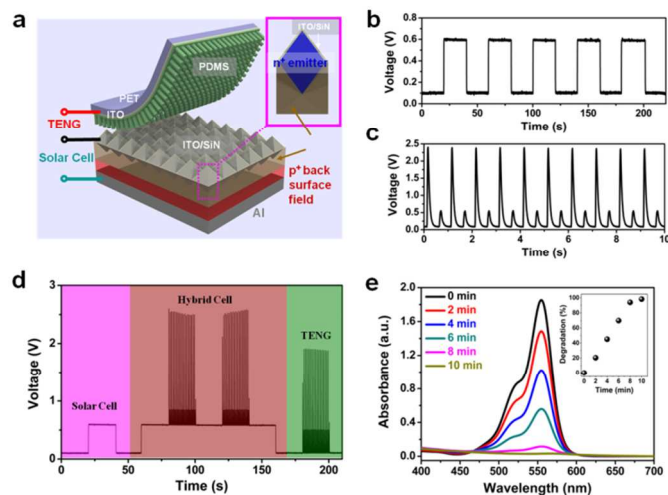


**Fig. 13** The hybrid energy cell composed of TENG and Si solar cell. (a) Schematic diagram of the fabricated hybrid energy cell composed of a TENG and a Si-based solar cell. (b) The output voltage of the fabricated Si solar cell. (c) The output voltage of the TENG after the output signal was rectified. (d) The output voltage of the hybrid solar cell and TENG (after rectification) for simultaneously harvesting solar and mechanical energies. (e) Absorption spectra of the RhB solution under the same time intervals. The inset shows the plot of degradation percentage versus the electrodegradation time. Reproduced with permission from American Chemical Society.<sup>118</sup>

A typical example of this type of AC-DC hybrid cell is a silicon-based hybrid cell, which is composed of a conventional Si solar cell and a TENG.<sup>118</sup> As shown in Fig. 13a, the Si solar cell is a typical multi-layered structure with a p+ back surface field layer, a p-type Si layer, a n+ emitter layer, a SiN film, Ag grids, and the transparent ITO electrode. The protection layer on top of pyramid Si microstructure was replaced as a thin layer film of PDMS nanowires deposited with ITO electrode. Then, the ITO-coated PDMS thin film and the conducting Si surface compose the TENG. The PDMS layer can serve as both the protection layer for the solar cell with high transparency, and the effective triboelectric layer for the TENG. Both their output performances were measured instantaneously. The open-circuit voltage and short-circuit current density of the solar cell are 0.6 V and 35 mA/cm<sup>2</sup>, respectively. The corresponding energy conversion efficiency is about 16%. The TENG presents an AC output signal with a pulsed voltage of 2.5 V, and it can be rectified to integrate with the output of the solar cell, as shown in Fig. 13b-c. Figure 13d displays the output voltage measurement for each generator both individually and in serial connection. The peak output voltage of the hybrid cell can be optimized by the contribution of the

TENG, and it can be further enhanced to 12 V by tuning the separation distance of the TENG.

On the other hand, a high output current of up to 18 mA was maintained from the solar cell. The potential application of the hybrid cell has been demonstrated for electrochemical degradation of Rhodamine B (RhB) and directly driving portable electronics. The electrochemical degradation of pollutants for waste water treatment has been extensively reported, all of the experiments require external power sources for the electrocatalytic oxidation process. The traditional power supply was entirely replaced by the hybrid cell to make this process self-powered. The UV-vis absorption spectral of the RhB solution was monitored during the electrochemical degradation process, as shown in Fig. 13e. It can be observed that the characteristic absorption peak intensity at 554 nm decreases with increasing degradation time, indicating the reduction of RhB concentration in the solution. The degradation percentage can reach up to 98% within 10 min, and a control experiment was carried out to exclude other possible factors and finally confirm that the degradation was due to the energy provided by the hybrid cell.

Besides this work, Yang and his co-workers also developed various types of AC-DC hybrid cell, which were based on the hybridization of TENG with thermoelectric cell<sup>109</sup> and electrochemical cell,<sup>110</sup> respectively. Zheng *et al.* also introduced hybrid cell composed on water-TENG and solar panel for simultaneously harvesting raindrops and solar energies.<sup>106, 119</sup> The major advantage of this type of hybrid cell is the combination of both high open-circuit voltage of the TENG with AC manner, and the high short-circuit current of the other energy cell with DC current. With such integration, the shortcoming of the TENG (low output current) was successfully improved by providing a complimentary power source.

## 5.2 TENGs for self-powered systems

The ultimate goal of nanogenerators is to build up self-powered systems, in which multifunctional electronic devices can be powered up by the nanogenerators through collecting ambient mechanical energies. To achieve this goal, energy storage devices and power transformers are indispensable to store the harvested energy and to regulate the output power into a constant DC power to drive electronic devices. The concept of self-powered system has been applied in many fields owing to the high output of TENGs, including powering portable electronics, electrochemical reactions, electronic logical circuitry, sensor networks, biomedical devices, etc.

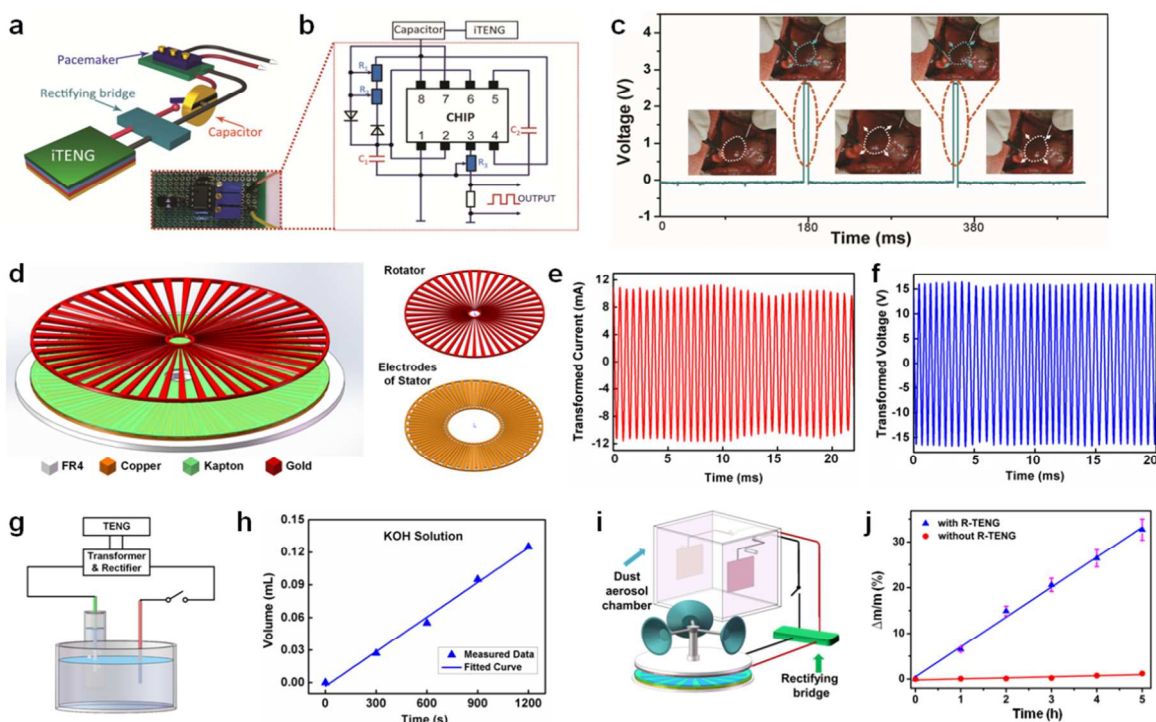


**Fig. 14** The applications of TENGs in self-powered pacemaker, water splitting, and air cleaning. (a) Scheme diagram of a self-powered prototype pacemaker.<sup>120</sup> The inset is a photograph of the pacemaker. (b) Circuit diagram of the prototype pacemaker ( $R_1 \approx 0\text{-}50\text{ k}\Omega$ ,  $R_2 \approx 0\text{-}200\text{ k}\Omega$ ,  $R_3 \approx 0\text{-}100\text{ k}\Omega$ ,  $C_1 = 10\text{ }\mu\text{F}$ ,  $C_2 = 0.01\text{ }\mu\text{F}$ ). (c) The measured voltage profile when stimulating the heart of the rat by self-powered pacemaker (insets: photographs of the heartbeat of the rat regulated by self-powered pacemaker). (d) Schematic illustrations of the disk TENG for self-powered water splitting.<sup>121</sup> (e) The short-circuit current and (f) the open-circuit voltage of the disk TENG after applying a transformer. (g) Schematic diagram of the TENG-driven water splitting system. (h) The measured  $\text{H}_2$  production volume as a function of time. (i) Schematic diagram of the self-powered dust particles precipitation system driven by a disk TENG.<sup>122</sup> (j) Weight increase of the copper mesh with and without R-TENG. The distance between collecting plates is 15 cm. Reproduced with permission from Wiley and Elsevier.

A sustainable power source is critical for the operation of implanted biomedical devices, especially considering the limited lifetime of the traditional battery power supply, since the replacement of drained batteries usually require additional surgery with more risk and pain to the patients. In this regard, Zheng *et al.* developed the first in-vivo biomechanical energy harvesting system with an implanted triboelectric nanogenerator (iTENG) to power up a prototype pacemaker by harvesting energy from the periodic breathing of a living rat.<sup>120</sup> The schematic diagram of this self-powered pacemaker is shown in Fig. 14a, which is composed of an iTENG, a bridge rectifier, a capacitor, and a pacemaker. The effective triboelectric materials for the iTENG are PDMS with gold electrode and aluminum film, and it is operated at vertical contact-separation mode. The output performance of the iTENG was measured under the mechanical deformation from both a mechanical

shaker and the periodical inhalation of the rat. The averaged output voltage and current in the latter test was 3.73 V and 0.14  $\mu\text{A}$ , respectively, due to small deformation and limited device size, but the output is still considerable for powering most implantable devices or microchips. To demonstrate the self-powered application, a prototype pacemaker was fabricated based on a 555 timer IC (Fig. 14b). It outputs a continuous stream of rectangular pulses at a specified frequency, and the parameters of the output pulse are tuned by the resistors and capacitors in the circuit. In the self-powered system, the AC output from the iTENG was transformed to a pulsed output by the full-wave rectifying bridge and stored in the capacitor. The capacitor could be charged from 2 to 3 V within 275 min (equivalent to 13750 breathing cycles), and the self-powered pacemaker was realized with regulated frequency (Fig. 14c). Furthermore, the iTENG can be driven by many other live organs,

like the diaphragm and the liver to obtain greater magnitude of deformation and thus higher performance.

### 5.3 TENG for self-powered electrochemistry

Since the first invention of TENGs, many applications in electrochemical reactions have been demonstrated, such as pulsed electro-deposition, electrochemical degradation, metal anticorrosion, and electrochromic devices. As the output performance is gradually improved, more and more potential applications that require higher current input could be possible. Self-powered water splitting is one typical example. A high current flow is highly desired for fast production rate of hydrogen, but an electrical potential of several volts will be enough to initiate the electrochemical splitting. Tang *et al.* fabricated a rotary-disk-based TENG that consists of a rotator and a stator.<sup>121</sup> As exhibited in Fig. 14d, the rotator is a collection of radial-arrayed sectors with each sector unit having a central angle of 1°. The stator consists of three components: a layer of Kapton as the triboelectric material, a layer of two complementary-patterned electrodes separated by fine trenches, and an underlying epoxy glass cloth laminate sheet as the substrate. The working principle of this rotary TENG has been reported previously. With a rotation speed of 600 rpm, the  $V_{OC}$  and  $I_{SC}$  of the TENG can reach up to 240 V and 1 mA. The output current can be further boosted to 11 mA by a power transformer, and the voltage is reduced to 17 V, with a transforming efficiency of 78% (Fig. 14e-f). The transformed output terminals were directly connected to the cathode and anode for the water splitting unit (Fig. 14g). Pt wires were selected as both electrodes, and 30% (w.t.) KOH solution was utilized as the electrolyte. With the potential applied by the TENG, O<sub>2</sub> and H<sub>2</sub> were produced at the anode and the cathode, respectively. In order to collect the produced H<sub>2</sub>, the cathode was inserted into a top-sealed tube. The volume of H<sub>2</sub> production with increased time was illustrated in Fig. 14h, and the linear relationship indicates a production rate of  $6.25 \times 10^{-3}$  mL min<sup>-1</sup>. This hydrogen production rate was tested with various rotation speeds and electrolyte solutions, and it was found that the production rate increase almost linearly with increasing rotating speed, and a higher production rate could be achieved with a 30% KOH solution, which might be due to higher concentration and lower resistance. Moreover, the splitting of pure water could even be completed with the high output voltage of the TENG without a transformer, while it could not be acquired by a 10 V electrochemical workstation, for the large resistance of pure water. Finally, the concept of “self-powered water splitting” was successfully demonstrated by TENG driven by water flow. In this experiment, the TENG was mounted to a

miniaturized water turbine, and then driven by a tap water flow of 3 L min<sup>-1</sup>. A capacitor of 1000 μF was employed as a charge reservoir, and it was charged from 1.7 V to 4.5 V in 60 min. As a result, a hydrogen volume of  $0.3 \times 10^{-3}$  mL was generated, which corresponded to a total charge transfer of 2.57 mC. This work presents a self-powered water splitting system, and introduces an effective approach for in-situ hydrogen generation without an external power source.

The rotary TENG can be further applied in self-powered cleaning of air pollution. In this work demonstrated by Chen *et al.*, a similar rotary TENG was connected to a miniaturized wind cup system to scavenge energy from wind blowing.<sup>122</sup> With a wind speed of up to 15.1 m/s (7 BF), the generated electricity or potential difference could be utilized to remove the SO<sub>2</sub> or dust in air. The removal of SO<sub>2</sub> was based on its electrochemical reactions with the current flow generated by the wind-driven TENG, which turned the SO<sub>2</sub> into H<sub>2</sub>SO<sub>4</sub> in the solution. As a result, the reaction was verified through a number of factors, including the PH value in the underlying solution, the generation of precipitation in a BCl<sub>2</sub>-HCl solution, and the degree of corrosion of a copper mesh. On the other hand, the removal of dust relied on electrostatic precipitation initiated by the electrical field between two plate electrodes, as shown in the schematic of Fig. 14i. Since the dust aerosol was either positively or negatively charged due to electrification between air and particles, charged particles would be drawn onto the corresponding plate electrodes by columbic force, and the amount of dust removal could be measured by the weight accumulation of the plate electrode. With the control experiment as presented in Fig. 14j, the copper mesh could absorb 32.7% wt. of dust particles with a potential difference of 300 V provided by the TENG, while no obvious mass change could be observed with the same system without TENG connection. This research paves the way for new applications of self-powered electrochemistry in environmental protection, especially for air purification without applying additional power.

Recently, Yeh *et al.* demonstrated a self-powered smart window system based on motion-driven electrochromic reactions.<sup>123</sup> In this work, the self-powered smart window was realized through integrating an electrochromic device with a transparent TENG driven by blowing wind and raindrops. Driven by the sustainable output from the TENG, the transmittance of the electrochromic device presented reversible variations due to electrochromic redox reactions, and the maximum transmittance change could reach up to

32.4%, which was comparable to that operated by a conventional electrochemical potentiostat. This research is a substantial advancement towards next-generation power-efficient buildings.

## 6. TENGs as self-powered active sensors

The rapid development of internet of things (IoTs) requires wireless, multi-functional, and independent operation of sensor networks. Considering the large number and small scale of sensors, the implantation of traditional power supply will be a big challenge, and developing self-powered sensors that can employ the ambient environmental energy is highly desired. In this regard, the self-powered active sensors based on the TENGs will be an optimum solution. As a new power generation technology, the TENGs be used to convert mechanical energy into electricity; on the other hand, by analyzing the electrical output signals (including  $V_{OC}$ ,  $J_{SC}$ , frequency, etc) of the TENGs, the information of the mechanical input (magnitude, frequency) can be successfully retrieved. Since this sensing technology originates from the output signals of the TENG itself, no external power source is required to apply onto the device, which is a unique advantage over conventional sensor technologies. By correlating the mechanical input with many other parameters, a lot of prototypes have been realized for various applications, including pressure detection, motion sensing, acoustic sensing, environmental monitoring, security check, and many more.

### 6.1 TENGs as self-powered pressure/touch sensors

The output performance of a TENG is greatly affected by magnitude/frequency of the external mechanical stimuli, and the pressure applied onto the device is among the most critical parameters. Hence, the most straightforward application for TENG-based active sensors would be the quantification of external pressure/touch. The first proof-of-concept prototype was realized on a transparent flexible TENG, with the micropatterned plastic surface to enhance the triboelectric charge density.<sup>29</sup> The self-powered pressure sensor was enabled to sense gentle pressures like a water droplet (8 mg,  $\sim 3.6$  Pa in contact pressure) and a falling feather (20 mg,  $\sim 0.4$  Pa in contact pressure) through relative deformation between two polymer sheets by external pressure. To obtain a more quantitative understanding of the contact-mode TENG based active pressure sensor, the TENG-based active pressure sensor was further developed and comprehensively characterized to reveal its basic sensing capabilities. In this work, the gap distance was employed as a critical factor to correlate the applied pressure and the potential

difference across the two electrodes of the TENG. Based on both numerical calculation and experimental measurement, it was revealed that the relative variation of the  $V_{OC}$  of the TENG should be expected to show direct linear relationship with the applied pressure. Therefore, the  $V_{OC}$  was a reliable parameter for static measurement of the magnitude of the external pressure, while the  $J_{SC}$  was able to provide its dynamic information (i.e. loading rate). The characterization of the pressure sensor indicated a high sensitivity of  $0.31 \text{ kPa}^{-1}$ , with a low-end detection limit of  $\sim 2$  Pa, as well as excellent stability of over 30,000 cycles. Finally, a  $6 \times 6$  pressure sensor array was integrated onto a common aluminum electrode for instantaneously mapping the applied pressure distribution, which was realized through multi-channel measurement and presented as a contour plot of the output profile of all the TENG units.<sup>40</sup> This design will open up many potential applications in electronic skin and touch screen. A similar design was proposed by integrating an array of single-electrode TENGs, and the pressure mapping could be visualized the illuminating the LEDs using the power output from each individual TENG unit.<sup>124</sup> Future works are anticipated to enhance the spatial resolution of tactile imaging through microelectronic fabrication and advanced structural designs.

The performance of such active touch sensor was further improved by Zhu *et al.* through a self-powered tactile sensor based on flexible thin film materials.<sup>64</sup> The schematic structure of this device is illustrated in Fig. 15a, in which a layer of polyethylene terephthalate (PET) deposited with ITO electrodes on both sides formed the structural backbone of the triboelectric sensor (TES). Fluorinated ethylene propylene (FEP) thin film was applied on top as a triboelectric layer for contact electrification with a foreign object. Vertically aligned polymer nanowires (PNWs) were created on the FEP layer (Fig. 15b) to assist the generation of triboelectric charges. To evaluate the performance of the TES to a contact event, a square-shaped TES (Fig. 15c) was utilized to detect a piece of metal by cyclic contact and separation. As presented in Fig. 15d, at an applied pressure of 0.03 kPa, the TES produced a uniform output voltage with the maximum magnitude of 35 V. As the contact pressure increased, the output voltage was raised to 50 V when the contact pressure approached 10 kPa (Fig. 15e). This increasing behavior was attributed to the increase of effective contact area between the metal object and the TES. The voltage-pressure curve exhibited two distinct slopes, which was in agreement with the previous contact-mode active pressure sensor. In the low-pressure region ( $< 0.15$  kPa), an exceptional pressure sensitivity of 44 mV/Pa

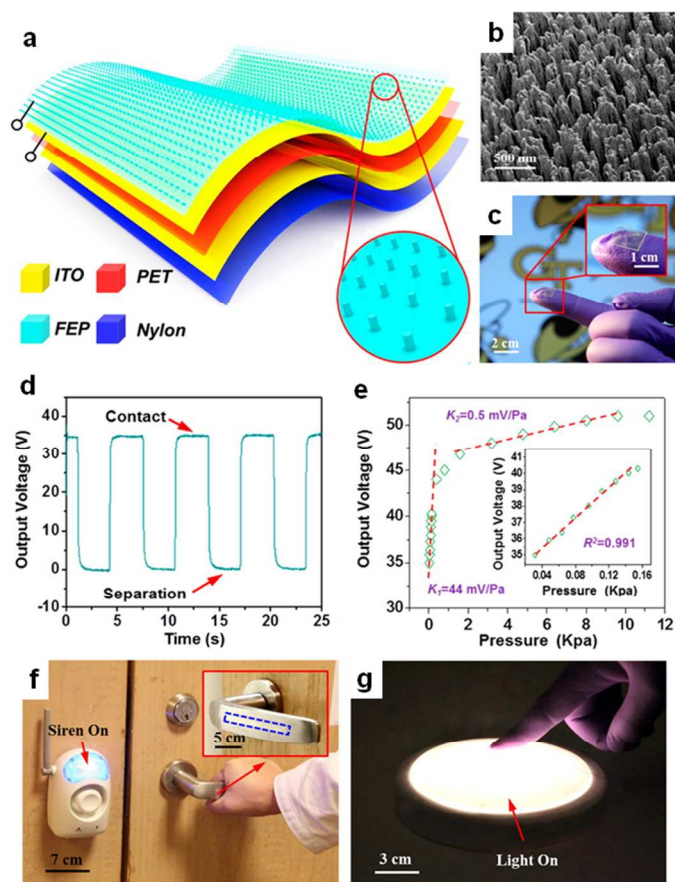


**Fig. 15** A self-powered, flexible, and ultrasensitive tactile sensor.<sup>64</sup> (a) The schematic structure of the tactile sensor. (b) The SEM image of the polymer nanowires created on the surface of the FEP thin film. (c) The photograph of the tactile sensor for measuring the contact event from a foreign object. (d) The measurement of open-circuit voltage with a cyclic contact force of 20 mN. (e) The summarized results of the output voltage under different contact pressures. Inset: an enlarged view of the summarized results at low pressure region. (f) A photograph showing that the TES was integrated with a signal processing circuit to turn on the siren alarm when a human hand touched the door handle. (g) A photograph showing that the TES was integrated with another signal processing circuit to turn on light when it was contacted by human fingers. Reproduced with permission from American Chemical Society.

was obtained, corresponding to a sensitivity factor of  $0.09\% \text{ Pa}^{-1}$ . In the relatively high-pressure region ( $> 2 \text{ kPa}$ ), the pressure sensitivity dropped to  $0.5 \text{ mV/Pa}$ . It was proposed that the two-region behavior was related to the enhancement effect from the PNWs. The dependence of its touch sensitivity on various factors was systematically tested, such as the applied pressure, the size of the touching object, and the length of PNWs. To demonstrate the

practical application of the tactile sensor, a complete wireless sensing system was developed through integrating the TES with a signal-processing circuit. The system relied on the output voltage from the TES to trigger an IC timer that controlled a wireless transmitter for remotely switching a siren alarm. As indicated in Fig. 15f, the sensing system immediately started operation once a human hand touched the door handle. Through substituting other functional electronics for the wireless transmitter in the circuit, the sensing system could be adopted for more purposes. For example, a touch-enabled switch for a panel light was successfully developed and shown in Fig. 15g. The TES in this work had a number of other unique advantages, including ultrahigh sensitivity, self-generated output, location independence, and outstanding robustness. In addition, the TES was generally applicable to objects made from various materials, indicating the widespread adaptability of the TES in a variety of circumstances.

Most recently the TENG was integrated with a passive resistive pressure sensor, and the whole device was a sandwiched structure with an ultrahigh pressure sensitivity of  $204.4 \text{ kPa}^{-1}$ . In this work, both active and passive pressure sensing was realized with the same device, and the resistive pressure sensor could be powered by the TENG.<sup>125</sup> The entire sensing system also exhibited very low detection limit, rapid response time, and long-term stability. A portable visualization pressure sensing system was also built to convert the pressure information into a visual display directly. The basic concept and structure of the TENG-based self-powered pressure/touch sensors can be utilized for a variety of applications, such as healthcare and security. Several typical examples include a membrane-based triboelectric sensor for health monitoring, a skin-friendly human-machine interfacing, and a paper-based anti-theft sensor.

## 6.2 TENGs as self-powered motion/trajectory sensors

A mechanical motion can be described with a series of parameters, like displacement, velocity, acceleration, etc. Sensors for detection of these parameters are vitally important for mechanical systems with moving parts. TENGs have been developed to generate electricity from different types of mechanical motions, such as linear sliding, rotation, and rolling. Since the frequency and amplitude of the generated electrical signals are all directly related to the parameters of the input mechanical motions, the TENGs can play the role of self-powered active motion sensors. Even if such motions are

located in concealed locations, TENGs can be utilized to track the trajectory and detect the instantaneous parameters of the motions.

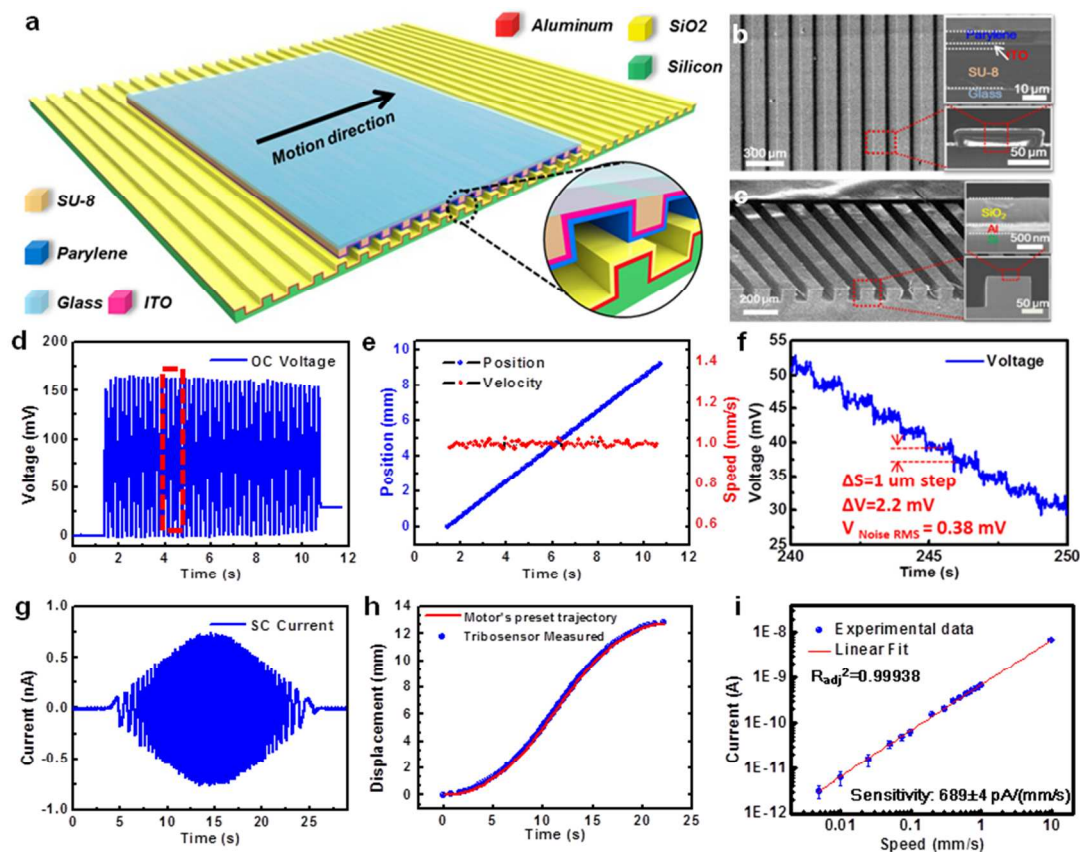


**Fig. 16** Micro-grated triboelectric nanogenerator as nanometer resolution self-powered linear displacement sensor.<sup>54</sup> (a) Schematic showing the structure of a TENG-base self-powered displacement sensor, with a pair of microgratings, the inset illustrates the detailed information of layers. (b) SEM images of the top micrograting with glass slide substrate. The insets show the cross section: the ITO layer on top of the patterned SU-8 photoresist serves as the top electrode, and the outmost layer is Parylene film serving as electronegative triboelectric layer. (c) SEM images of the bottom micrograting. The insets show the cross section profile: the etched Silicon is coated with Al as bottom electrode and SiO<sub>2</sub> as electropositive triboelectric layer. (d) The OC voltage signals acquired from a displacement of 9.2 mm at a preset speed of 1 mm s<sup>-1</sup>. (e) The real time displacement and speed derived from the measured voltage signal. (f) Step motion with 1 μm per step in the sensitive region (10–190 μm) can be clearly resolved through the OC voltage signal. Given the RMS value of noise (0.38 mV), and the voltage change corresponding to 1 μm step motion (2.2 mV), the resolution can be calculated to be 173 nm. (g) The SC current signals acquired from a non-uniform motion (decelerate – uniform speed – deceleration). (h) The preset motor's trajectory and the real time displacement detected by the motion sensor. (i) A plot of SC current as a function of motion speed from 5 μm s<sup>-1</sup> to 10 mm s<sup>-1</sup> with a fitted sensitivity of 689 ± 4 pA (mm s<sup>-1</sup>). Reproduced with permission from Wiley.

Zhou *et al.* developed a self-powered, one-dimensional displacement and speed sensor with high spatial resolution, large dynamic range and long detecting distance.<sup>54</sup> As shown in Fig. 16a, the motion sensor consisted of two micro-grating layers with identical patterns. The bottom layer was an etched silicon wafer coated with aluminum as the bottom electrode and silicon dioxide as one of the triboelectric material to generate positive charges; the top layer was a patterned SU-8 film on a glass slide as supporting

substrate, which was subsequently coated with ITO and Parylene film as the top electrode and the other triboelectric material to generate negative charges, respectively. The detailed structure of the as-fabricated devices can be found in the SEM images in Fig. 16b-c, respectively. The relative motion between two gratings results in periodic separation of two micro-grated triboelectric materials that are oppositely charged through triboelectrification. As a result, an alternating electric signal between the two electrodes placed was

detected due to electrostatic induction. During the movement, the  $V_{OC}$  measured between the two electrodes (Fig. 16d) alternated between 0 and  $\sim 160$  mV periodically, and the real time displacement could be calculated by counting the number of voltage peaks and multiplying the number with the width of each grating (200  $\mu\text{m}$ ). As presented in Fig. 16e, the detected displacement increased linearly with time, and the real time motion speed could also be calculated by dividing the grating width by the time interval between two adjacent peaks. Starting from a status with complete overlap, a step motion test with each step of 5  $\mu\text{m}$  was performed to investigate the resolution of the displacement sensor. The sensitive region was found to be from 10  $\mu\text{m}$  to 190  $\mu\text{m}$ , where each step motion of 1  $\mu\text{m}$  could be clearly identified from the voltage variation, as displayed in Fig. 16f. The change of the voltage for each step was about 2.2 mV, and the root mean square (RMS) of the noise  $V_{noise}$  at 1 Hz is 0.38 mV. Consequently, the displacement resolution at bandwidth of 1 Hz was determined to be 173 nm. The measured  $I_{SC}$  could also serve as the sensing signal for the displacement and speed, as shown in Fig. 16g. The real time displacement could be derived by counting the number of zero-crossings, and the measurement result matched very well with the preset trajectory (Fig. 16h). On the other hand, the amplitude of the  $I_{SC}$  also helped to quantitatively determine the real time speed, given small aspect ratio of the dielectric layer. Figure 16i shows the plot of the magnitude of the output current with motion speed from 5  $\mu\text{m s}^{-1}$  to 10  $\text{mm s}^{-1}$ , and a linear fitting indicated its sensitivity of 679  $\text{pA}/(\text{mm s}^{-1})$ . The resolution in dynamic speed detection was 1.2  $\mu\text{m s}^{-1}$  given the RMS value (0.8 pA) of the noise. The resolution for both displacement and speed sensing can be further improved by reducing the grating period. This new approach of self-powered displacement/speed sensing distinguishes itself from the existing technologies by nanometer resolution, long detecting range and non-optical compacted structure, showing extensive potential applications in automation, manufacturing, and process control, etc.

The first prototype of single-electrode TENG has been demonstrated to serve as self-powered tracking system with the integration of an array structure. Besides, a self-powered single-electrode-based displacement sensor has been developed by using grating linear array of Al electrodes for detecting the motion of an object without an external power source.<sup>56</sup> The output voltage signals from 16 Al electrode channels were recorded in real time as a mapping Figure. The motion direction and location of the object can be obtained by analyzing the measured mapping figures. In another

work by Su *et al.*, a series of single-electrode triboelectric sensors (SE-TES) was integrated into a one-dimensional array of tube structures consisting of tube-shaped PTFE thin film and grating copper electrodes for tracking the motion status (location, speed) of a steel ball moving inside the tubing.<sup>66</sup> Yi *et al.* continued to extend this structure into a two-dimensional array of the SE-TES to actively detect the position, displacement, velocity, and acceleration of a moving object in real time.<sup>65</sup> The detected velocity and acceleration of the moving object had an average error of  $\sim 0.265\%$  and  $\sim 2.5\%$ , respectively. The velocity could also be detected by utilizing the amplitude of the short-circuit current, which had a sensitivity of  $\sim 887 \text{ pA}/(\text{cm s}^{-1})$ . Additionally, LED illuminations were employed as real-time indicators to monitor the motion of a sliding object and walking steps of a human. Han *et al.* fabricated a self-powered velocity and trajectory tracking sensor (VTTS) array with higher resolution. A self-powered VTTS arrays (9 $\times$ 9 pixels) with low-node mode had realized the real-time tracking of position, velocity, acceleration and trajectory for a moving object by visual observation.<sup>126</sup> With a simply electrode weave technique, a high-resolution VTTS with 41 $\times$ 41 pixels on an active size of 1 $\times$ 1  $\text{cm}^2$  was obtained and it could detect a tiny displacement of 250  $\mu\text{m}$ . A self-powered acceleration sensor based on single-electrode spherical TENG was developed with a detection sensitivity of about 15.56  $\text{Vg}^{-1}$ .

Rotating motion also widely exists in mechanical components, such as turbines, automobiles, gears, etc. Self-powered quantification of a rotation motion conveys equal significance with that of a linear motion. On the basis of the lateral-sliding mode of TENGs, a disk TENG with segmental structures for harvesting rotational mechanical energy has been invented. Enabled by the distinct relationship between the electrical output (its frequency and amplitude) and the rotational speed, the disk TENG could also serve as a self-powered angular speed sensor for rotation motions.<sup>49</sup> Later on, a free-rotating disk TENG (FRD-TENG) was developed for improved output performance and better device durability, and it further extended the application of a rotary TENG as a self-powered rotation sensor. In this work, FRD-TENG was enabled to work in noncontact conditions, and the output magnitude decreased as the vertical distance between two disk planes was elevated.<sup>81</sup> On the other hand, the rotation speed could be determined by both the magnitude and frequency of the  $J_{SC}$ . Therefore, the information about two important parameters of a rotary motion could be solely determined by the measured profiles of the  $J_{SC}$ . Based on this

principle, the FRD-TENG could be employed as a self-powered mechanical sensor in automobiles to detect both the radial and axial movement of a braking pad at the same time. This two-parameter monitoring approach provided us insights on the application of nanogenerators in self-powered active sensors and exhibited unique advantages than the existing single-parameter active sensors. Also, through combing the structures of cylindrical TENGs that can serve as self-powered rotation sensor and case-encapsulated TENGs that can serve self-powered linear sliding sensors, a dual-mode, self-powered velocity sensor for rectified linear and rotary motions was reported.<sup>55</sup> The output signals were integrated with a digital circuit and a microcontroller unit (MCU), and they could be directly processed into velocity information. Linear speeds of 0.1–0.6 ms<sup>-1</sup> and rotary speeds of 125–700 rpm were simultaneously measured with high stability.

### 6.3 TENGs as self-powered vibration/acoustic sensors

Vibration is a unique type of mechanical motion available almost everywhere in engines, buildings, aircraft, and infrastructures, which reflects the operation status of machineries. Taking advantage of vibration-induced periodical contact and separation of two triboelectric surfaces, a contact-mode TENG can be employed for both harvesting vibration energy and detecting the magnitude, frequency, and location of a vibration source. A few prototypes have been developed in this field of TENG-based self-powered vibration sensor. One typical example is the 3D spiral structure, which was composed of a conical-shaped spring, a seismic mass loaded on the spring, and another acrylic plate fixed beneath the seismic mass.<sup>127</sup> The triboelectric materials were attached on the surfaces between the seismic mass and the underlying plate, and the spiral triboelectric nanogenerator (STENG) was operated by the oscillation of the spring stimulated by an external vibration. The STENG was further demonstrated for vibration source positioning on a wood board, and three STENGs were installed on its three corners, respectively. The output signals were recorded once a vibration was incurred at a specified location on the board, and its position could be precisely tracked through monitoring the arriving time in the three different measurement channels and derived with simple calculations. The location error of this measurement was as low as 5.8%, which could be further reduced by increasing the sampling rate of the measurement system. Beside this work, several other structure designs have also been proposed for harvesting vibration energy, such as the harmonic-resonator-based TENG,<sup>31</sup> the 3D TENG with

broadband response,<sup>128</sup> the 3D stack integrated TENG,<sup>96</sup> the triple-cantilever-based TENG,<sup>34</sup> and the integrated rhombic gridding based TENG.<sup>36</sup> They all can be utilized as the self-powered active sensor to detect external vibrations.

Furthermore, to obtain a more quantitative and accurate amplitude measurement of vibrations, Wang *et al.* first developed a contact-based freestanding-triboelectric-layer mode triboelectric nanogenerator (CF-TENG), in which the vibration of the freestanding triboelectric layer between the two electrodes periodically changes the induced potential difference between the two electrodes and thus generate electricity in external load.<sup>79</sup> In such a structure with the lateral dimension of electrodes much larger than their vertical separation distance, the electricity generation had a linear relationship with the moving distance of the freestanding layer. The linear characteristic gave the CF-TENG the supreme capability of quantitatively sensing the amplitude of the vibration, as long as it within the small range. Specifically, at its resonant frequency, the CF-TENG showed very high sensitivity for even subtle vibration magnitude. For example, when the vibration amplitude was only 3.5 μm, the peak-to-peak value of the  $V_{OC}$  and the amplitude of the  $I_{SC}$  generated by the CF-TENG still had 0.54 V and 10 nA, respectively. Even when the vibration frequency was off the resonant frequency of the CF-TENG, it still showed good linear behavior at a high vibration magnitude of up to 15 mm.

Acoustic wave is a specific form of vibration ubiquitously existing in the environment, and the sensing of acoustic waves is vitally important not only for information technology, but also for the monitoring of equipment systems and environment. With the possibility of converting sound waves into electricity, TENGs could provide an effective approach for realizing the self-powered acoustic sensing. The first organic thin-film based TENG was developed to realize acoustic energy harvesting and self-powered acoustic sensing in a wide frequency range available in our daily life.<sup>44</sup> This acoustic TENG relied on a Helmholtz cavity with a size-tunable narrow neck on its back. The core part was in a circular shape and embedded as the flexible front plate of the cavity, as schematically depicted in Fig. 17a. When an external sound wave was incident on the core part of the device, the cavity structure would lead to a pressure difference and oscillation of the PTFE thin film (Fig. 17b). Assisted by the nanopores on the aluminum surface (Fig. 17c) and the nanowire structure on the PTFE thin film (Fig. 17d), contact electrification was enabled between aluminum and PTFE to scavenge the acoustic energy from sound waves. Moreover, a self-powered microphone

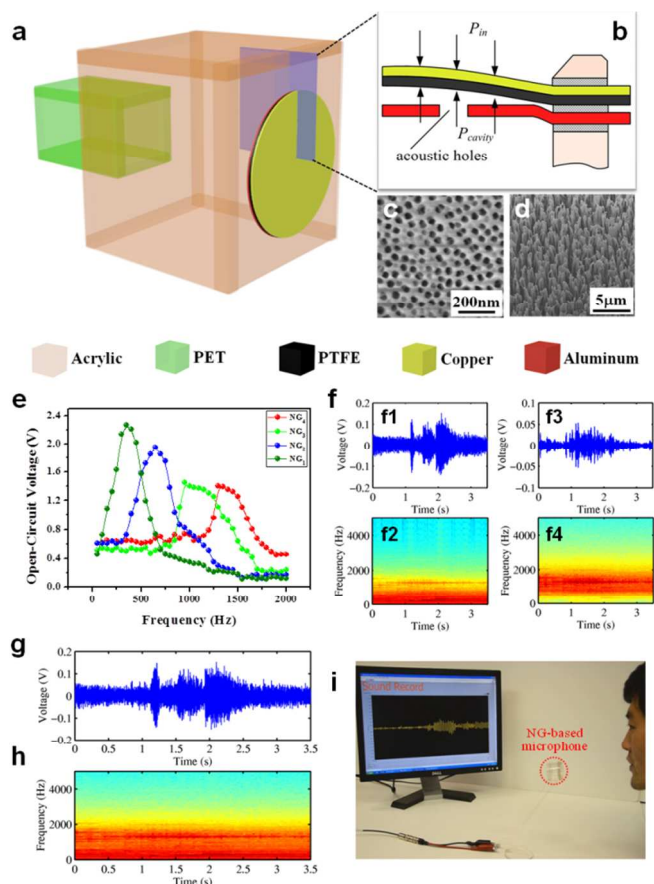


**Fig. 17** Triboelectric nanogenerator for self-powered active acoustic sensing.<sup>44</sup> (a) Sketch and (b) cross-sectional view showing the structural design of the triboelectric nanogenerators. (c) SEM image of nanopores on aluminum electrode. (d) SEM image of PTFE nanowires fabricated on the film surface by plasma etching, which largely increase the triboelectrification. (e-h) Demonstration of the TENG acting as a self-powered microphone. (e) Frequency responses from the nanogenerators array, which consists of four NGs with various designed natural frequencies, aimed to enhance the overall working bandwidth. (f1, f2) Sound waveforms of the signals acquired by NG1 and NG2, respectively. (f3, f4) Short-time Fourier transforms of the acquired signals by NG1 and NG2, respectively. (g-h) Sound waveform and corresponding short-time Fourier transform of the signals acquired by the array of the NGs. (i) Photograph that shows a NG is working as a self-powered microphone for sound recording. Reproduced with permission from American Chemical Society.

was demonstrated as an application of the TENG-based self-powered acoustic sensor. As demonstrated in Fig. 17e, four TENGs with a series of dimensions corresponding to distinct resonant frequencies were employed to widen the overall working bandwidth from 10 to

1700 Hz, which enabled the superior performance of the TENG for sound recording. The time domain waveforms of the recorded sounds from NG<sub>1</sub> and NG<sub>4</sub> are shown in Figs. 17f1 and f3, respectively. With a natural frequency of 350 Hz, the waveform of NG<sub>1</sub> was smoother owing to its dominant response to lower frequency components from 10 to 600 Hz, while the waveform of NG<sub>4</sub> with a natural frequency of 1400 Hz is rougher, due to its dominant response to the higher frequency components from 1100 to 1700 Hz, as shown in Figs. 17f2 and f4, which was the corresponding short-time Fourier transform (STFT). In order to reconstruct the original sound, the acquired acoustic signals were weighted according to the relative amount of information available from each source. The waveform of the reconstructed signal and its corresponding STFT are illustrated in Figs. 17g and h, respectively. The frequency components of the reconstructed signal covered all the frequencies ranging from 10 to 1700 Hz. Figure 17i shows an as-fabricated TENG working as a self-powered microphone for sound recording. The TENG in this work could also serve as a sound source locator, with similar working principle as the spiral TENG mentioned above. The proposed acoustic sensors in this work have extensive applications in fields such as military surveillance and reconnaissance, intruder detection, sniper localization, underwater acoustics, and auto talker detection in a web conferencing.

Furthermore, a self-powered acoustic source locator was also demonstrated with high sensitivity and adaptive in underwater environment. Three dimensional acoustic source positioning was also realized with the structural design well packaged in a cube framework.<sup>129</sup>

It is worth mentioning that Fan *et al.* further improved the performance of self-powered sound recording on the basis of an ultrathin, rollable, and paper-based TENG, which was capable of producing a maximum power density of 121 mW/m<sup>2</sup> and 968 W/m<sup>3</sup> under a sound pressure of 117 dB<sub>SPL</sub>.<sup>43</sup> The superior feature due to its structural novelty enabled it to harvest acoustic energy from portable electronics, and the generated electricity could charge a capacitor at a rate of 0.144 V/s.

In its demonstration as a self-powered microphone, some unique features like broad working bandwidth, structural rollability, and directional independence were successfully conveyed. The novel device structure can be extensively applied to a lot of circumstances for sensing purposes, including wearable and flexible electronics, military surveillance, jet engine noise reduction, low-cost implantable human ear, and wireless technology applications.

#### 6.4 TENGs as self-powered chemical/environmental sensors

As discussed in the previous chapters, a key factor that determines the output performance of a TENG is the triboelectric charge density generated on the material surface upon contact electrification. Surface modification of certain chemical species and alteration of environmental factors will greatly affect the triboelectric charge density and thus the output power. Therefore, by monitoring the change of its output performance, a properly-designed TENG can serve as a self-powered chemical and environmental sensor for detection of ion concentration, UV illumination, humidity, *etc.*

The first work was done by Lin *et al.* for the detection of  $\text{Hg}^{2+}$  ions.<sup>41</sup> In a typical contact-mode TENG, Au nanoparticles (NPs) were assembled onto the metal plate to improve the contact area, and the NPs were further modified with 3-mercaptopropionic acid (3-MPA) molecules with strong Au-S interactions. The  $\text{Hg}^{2+}$  ions in the buffer solution would be bound on 3-MPA molecules and the surface polarity of the metal plate would be subject to change, which then tuned the surface charge density accordingly. Hence, the detection of the  $\text{Hg}^{2+}$  concentration was enabled by real time monitoring of the TENG's output performance. A linear relationship between the relative variation of the  $J_{SC}$  and the concentration of  $\text{Hg}^{2+}$  ions indicated an effective detection range from 100 nM to 5 mM, and the selectivity of the developed system toward  $\text{Hg}^{2+}$  ion detection as compared to other metal ions was confirmed with a control experiment. Following this work, a similar self-powered chemical sensor was fabricated for catechin detection by utilizing  $\text{TiO}_2$  nanomaterial array as the probe and contact material.<sup>42</sup> The sensor also presented high sensitivity and good selectivity, with a detection limit of 5  $\mu\text{M}$ . TENGs based on water-solid electrification have been developed, which can serve as self-powered chemical and temperature sensors for the liquid. A self-powered active UV sensor was developed through integrating a built-in photodetector for UV light sensing with the TENG conformation.<sup>130</sup> The resistance of the built-in photodetector varied upon UV light irradiation with different intensities, which would consequently influence the measured output of the TENG from the two leads. In this way, the light intensity could be derived by monitoring the output of the TENG. An air-flow-driven TENG was developed as a self-powered humidity sensor with high sensitivity and simple fabrication.

Li *et al.* further expanded this concept to a more practical case for both self-powered phenol detection and its electrochemical degradation.<sup>131</sup> In this work,  $\beta$ -cyclodextrin ( $\beta$ -CD) was selected

both as a surface modification chemical to improve the performance of the TENG, but also as the recognition element for effective detecting phenol molecules in aqueous solution. The as-fabricated TENG and nanosensor had a multilayered structure with acrylic as supporting substrates, as schematically depicted in Fig. 18a. In this typical contact-mode TENG structure, the top layer was a piece of PTFE thin film coated with copper electrode, and the bottom layer was Ti foil with  $\text{TiO}_2$  nanowires grown on its surface through hydrothermal approach.  $\beta$ -CD molecules were then assembled onto the  $\text{TiO}_2$  nanowires as a surface chemical modification. The measured  $V_{OC}$  and  $J_{SC}$  were increasingly proportional to the surface concentration of  $\beta$ -CD till a saturation point of 80  $\mu\text{M}$  was reached, and the enhancement in electrical output was due to the charge transfer from  $\beta$ -CD to  $\text{TiO}_2$  (Fig. 18b). Assisted by the coordination effect between the hydroxyl groups in  $\beta$ -CD and the surface Ti atoms of the  $\text{TiO}_2$  nanowires, more surface charge transfer then took place at the contact area upon the triboelectrification between PTFE and  $\text{TiO}_2$ . Moreover, the  $\beta$ -CD molecule is composed of hydrophobic internal cavity and hydrophilic external surface, which allows it to form a host/guest inclusion complex via various guest molecules with suitable polarity and dimension. The cavity diameter of  $\beta$ -CD has been found to be the most appropriate size for the selective adsorption of phenol, which explains  $\beta$ -CD as a surface chemical modification for phenol recognition. To evaluate the experimental performance of the phenol sensor, phenol solutions with various concentrations but constant volumes (20  $\mu\text{L}$ ) were dropped onto the surface of  $\beta$ -CD modified  $\text{TiO}_2$  nanowires on a 4 cm $\times$ 4 cm TENG (Fig. 18c). The dependences of both the  $J_{SC}$  and  $V_{OC}$  on the phenol concentration were plotted in Fig. 18d and e, respectively, and it could be clearly found that both the  $J_{SC}$  and  $V_{OC}$  monotonically decreased with rising phenol concentration in a certain test range of 10-100  $\mu\text{M}$ . The decay of output was mainly attributed to a modified surface triboelectric behavior, for phenol would replace the position of  $\text{TiO}_2$  to contact with PTFE. In comparison with  $\text{TiO}_2$ , phenol molecules had a lower tendency to transfer the electrons to PTFE, resulting in lower output performance with increasing phenol concentration. The relative variation of the output voltage and current in response to varied phenol concentrations were plotted in Fig. 18f, from which a sensitivity of 0.02  $\mu\text{M}^{-1}$  could be derived.

Furthermore, control experiments were carried out to test the selectivity of phenol sensor as compared to other organic species. With a constant concentration of 50  $\mu\text{M}$  for all the testing organic

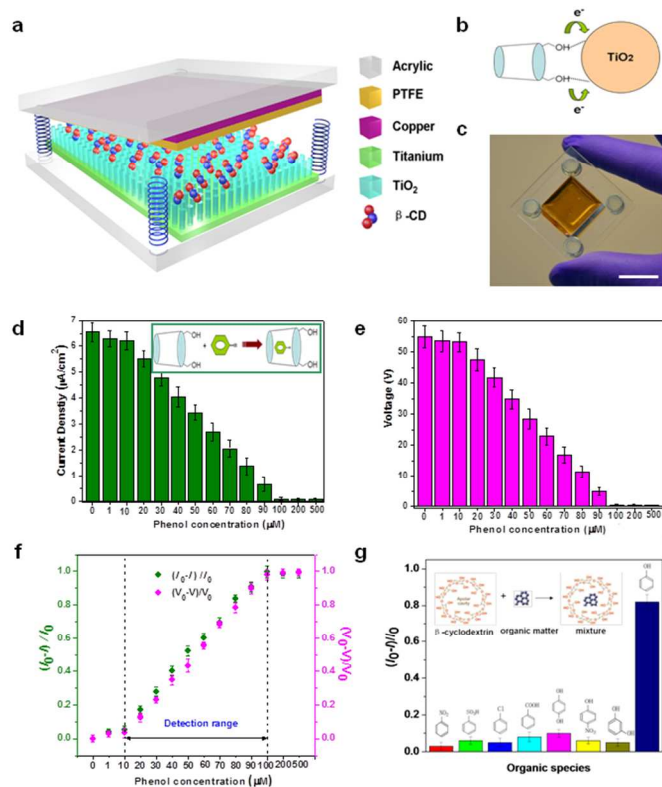


**Fig. 18** β-cyclodextrin improved TENG for self-powered phenol detection and electrochemical degradation.<sup>131</sup> (a) A sketch of the TENG with β-CD surface modification for phenol detection. (b) Schematic diagram for illustrating the charge transfer from the hydroxyl groups of β-CD to TiO<sub>2</sub> nanowires. (c) A photograph of the as-fabricated device for phenol detection. The scale bar is 2 cm. (d-e) Under a fixed 80 mM β-CD surface modification, dependence of the current (d) and voltage (e) output on the phenol concentrations. Inset shows the reaction mechanism between β-CD and a phenol molecule. (f) The sensitivity and detection range of the as-developed β-CD enhanced TENG for phenol detection in terms of both current and voltage output. (g) Selectivity of the as-developed β-CD enhanced TENG for phenol detection. Inset shows an illustration of the reaction mechanism between β-CD and different types of organic species. Reproduced with permission from Royal Society of Chemistry.

species, the obtained output current decrease from the phenol absorbed active sensor was much larger than that in the control groups, indicating the effective detection of phenol with excellent selectivity. Furthermore, the TENG in this work could also be utilized for self-powered electrochemical phenol degradation in a large container, owing to the high output performance of the TENG. This work not only provides a new and efficient pathway for

environmental chemical treatment, but also a solid “green” advancement in the fields of wastewater treatment, ecological sanitation, environmental degradation, monitoring, assessment and sustainability.

### 6.5 TENGs for self-powered human-machine interfacing and biomedical monitoring

Despite various types of mechanical inputs described in the previous chapters, human activity is also a kind of universally available mechanical source. Technologies in human-machine interfacing and biomedical monitoring have become more and more significant for rapid development of artificial intelligence and modern healthcare. Especially, a fatal weakness of the current authentication systems is that an identity thief/impostor can easily pass as the genuine owner with stolen personal identification information (e.g., password). Improvements regarding the issues can hardly be accomplished without having better identities that preferably cannot be easily separated from the owner of the computer. Here, the application of TENGs for biometric authentication can be harnessed to place an additional layer of stronger security on existing systems since they are intrinsic and harder to separate or mimic from the genuine owner. And they are featured as being inexpensive, less intrusive, and can be implemented easily on top of the current authentication systems without major modification. In a few recent works, human activities including keyboard typing, voice, or blood flow could be precisely recognized and recorded with personal patterns as effective identification criteria to current authentication system, which are important steps toward practical applications of TENGs and self-powered active sensors.

Keyboard is an indispensable input component for many personal electronics like computers and cell phones, and an advanced approach to provide multi-fold protection of electronic devices through a keyboard is highly desired for security purpose. Recently, Chen *et al.* invented an intelligent and self-powered keyboard as an advanced security safeguard against unauthorized access to computers.<sup>132</sup> Based on the triboelectric effect between human fingers and keys, the intelligent keyboard (IKB) could convert typing motions into localized electric signals that could be identified as personalized physiological information. The core part of the IKB was composed of multilayered transparent thin film materials to form a typical single-electrode TENG. A layer of polyethylene terephthalate (PET) was deposited with ITO electrodes

on both sides, and the top ITO was laminated by a layer of FEP as the triboelectric material for contact electrification with bare human

fingers (Fig. 19a). A nanowire structure was created on the FEP surface to enhance the effective contact area (Fig. 19b), which also introduced a self-cleaning surface. Figure 19c shows a photograph of a fully-assembled IKB with the same size as a commercial keyboard. The working principle of the IKB as an energy harvester was similar with the single-electrode TENG. The contact of human skin with the FEP surface would leave the finger positively charged, and the FEP negatively charged. The finger movement during typing would then induce change of the potential difference between the pair of ITO electrodes, driving electrons flow through the external load or data collection system. To demonstrate the capability of the IKB to differentiate the input of each key, all of the TENG units on the keyboard were separately connected to a multi-channel measurement system, and the output data of all channels were collected during the typing event on individual keys.

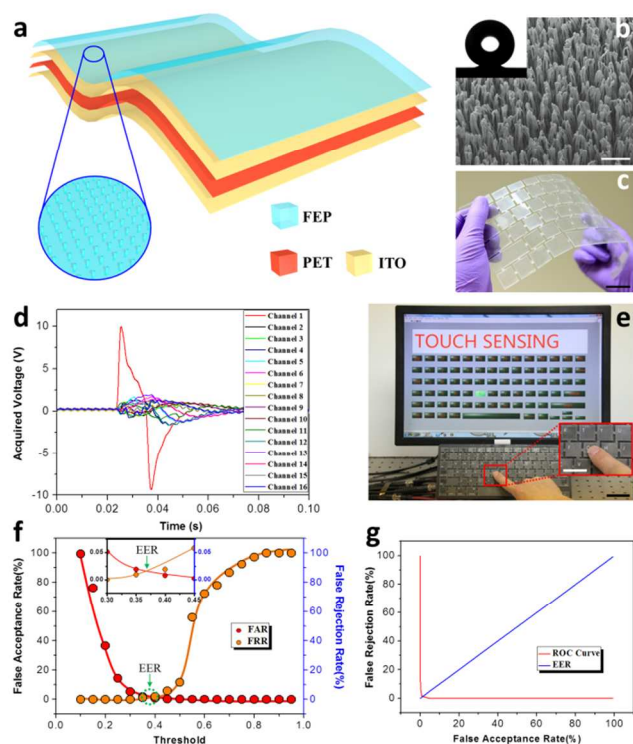


**Fig. 19** Personalized keystroke dynamics for self-powered human-machine interfacing.<sup>132</sup> (a) Schematic illustrations of the KFE. Inset: a enlarged schematic of FEP nanowires on the top surface. It should be noted that these drawings do not scale. (b) SEM image of FEP nanowires. Inset: contour of resting droplet for surface static contact angle measurement. The scale bar is 500 nm. (c) Photograph of a flexible and transparent KFE. The scale bar is 3 cm. (d) The system acquired output voltage signals when the key “T” was stroked. (f) An photograph demonstrated the IKB for the real-time keystroke tracing and recording. A continuously typing string “TOUCH SENSING” was recorded in real time without uncomfortable delay. The scale bar is 5 cm. Inset: enlarged view of the key “G” being stroked. The scale bar is 2 cm. (g) Evaluation of the performance of the biometric authentication system using triboelectrification enabled keystroke dynamics. The variation of FAR and FRR is related to the threshold. Inset: Enlarged view of the EER point, which indicates a remarkably low EER value of 1.34% at the threshold of 0.37. (h) Receiver operating characteristic (ROC) curve of the biometric authentication system using triboelectrification enabled keystroke dynamics. The false rejection curve is plotted as a function of the false acceptance curve. Reproduced with permission from American Chemical Society.

A typical output profile is presented in Fig. 19d, in which the channel located on the key struck by the finger exhibited an instantaneous voltage peak of about 10 V, which was much larger than that in the rest of the channels. The recognition of key striking could even be recognized by screening the data with a Pauta Criterion Method, and simultaneously visualized on the display without noticeable delay (Fig. 19e). As a novel approach for personalized typing verification and identification, the IKB was typed the word “touch” by three individuals for four times, and the characteristic electric signals (voltage and current) were analyzed through Discrete Fourier Transformation (DFT) to obtain their frequency features. It was found in the results that the frequency spectra of the voltage and the current from different individuals were distinct in term of the position and amplitude of the major signal components. Meanwhile, wavelet transformation was further carried out to simultaneously obtain both time domain and frequency domain features of the typing patterns. Based on DB4, the typing patterns could be identified by calculating the Pearson correlation coefficient of  $D_4$  and  $S_4$  components, which was utilized to quantitatively measure the correlation between the wavelet components of the individual typing patterns as follows

$$\gamma = \frac{\sum_{i=1}^n (t_i - \bar{t})(x_i - \bar{x})}{\sqrt{\sum_{i=1}^n (t_i - \bar{t})^2} \sqrt{\sum_{i=1}^n (x_i - \bar{x})^2}} \quad (7)$$

where  $n$  is the length of compared data sequence, and  $x$  is either the voltage or the current sequences after DB4. The Pearson correlation coefficient can be harnessed to express the uniqueness and permanence among individual typing patterns. A higher value about 0.85 represents a superior permanence of the typing patterns, while a

lower value around of 0.45 is indicative of excellent uniqueness among individuals.

Furthermore, to evaluate the performance of the IKB as an effective identifier, 104 randomly selected participants were invited to independently type the word “touch” for more than four times on the IKB in each accustomed manner. Subsequently, a collection of 104 individual typing patterns were divided into 52 client patterns and 52 impostor patterns. In the whole testing set of 104 typing patterns, the user template was composed of the 52 client patterns, and the performance of the authentication biometrics was characterized through two error rates: False Rejection Rate (FRR) and False Acceptance Rate (FAR). Here, the FRR is the probability that the system incorrectly rejects access of an authorized person, due to failing to match the user template. While FRR is the percentage of valid inputs which are incorrectly rejected. And the Pearson correlation coefficient was selected as the classification threshold to evaluate the behavioral biometric authentication system, as shown in Fig. 19f. The FRR was increasing with the elevated threshold, while FAR follows a reverse trend, and their intersection indicated the Equal Error Rate (EER) point. The presented biometric authentication system achieved a remarkably lower EER value of 1.34% at the threshold of 0.37, as compared with traditional techniques. In the meanwhile, the Receiver Operating Characteristic (ROC) curve is demonstrated in the Fig. 19g. Given its exceptional authentication capability, the IKB was able to identify the individual typing characteristics, making it practical as a highly secured authentication system based on behavioral biometrics.

TENG was further improved and extended into a bionic membrane sensor (BMS) with both security authentication and healthcare monitoring functionalities.<sup>133</sup> In this comprehensive work by Yang and co-workers, a wearable, light weight BMS was fabricated as a high performance pressure sensor to fulfill personalized detection of cardiovascular activity and human voice vibrations. The structure of the BMS is shown in Fig. 20a, which was a typical single-electrode TENG with PTFE and Nylon as the triboelectric pairs, which was designed to mimic a human eardrum. A layer of PTFE tympanic membrane was tented outwards at the level of the tip of an umbo (PET layer), which was centered at a Nylon layer deposited with ITO electrode. Two circular acoustic holes with diameters of 0.5 mm were punched through the multilayered structure, acting as communicating vessels to integrate the conical cavity with the ambient air (Fig. 20b). Nanowire structures were created on the PTFE surface to enhance the contact

area and the triboelectric charge density (Fig. 20c). The working principle of the BMS was similar with a single-electrode TENG,

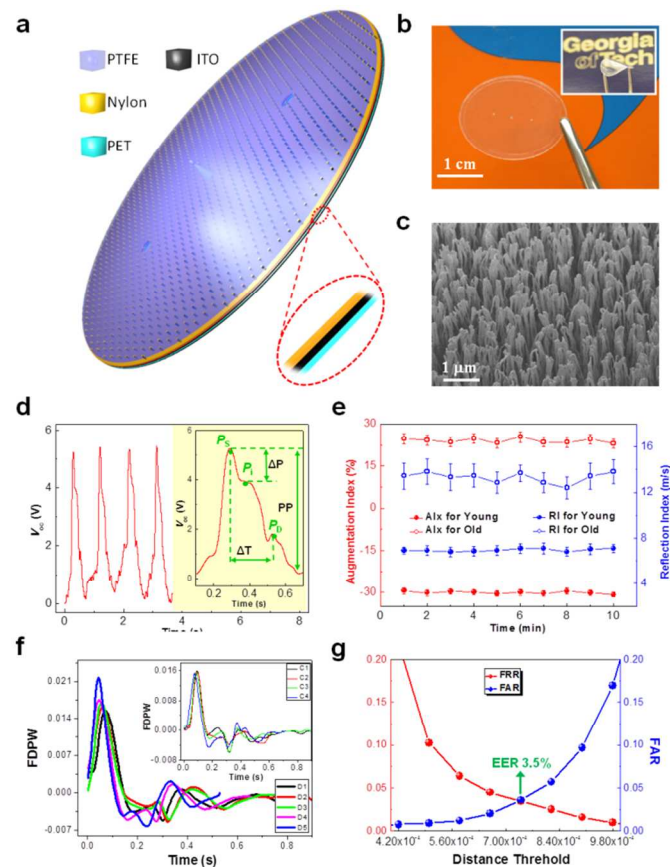


**Fig. 20** Eardrum-inspired active sensor for self-powered authentication and biomedical monitoring.<sup>133</sup> (a) Schematic illustrations of the bionic membrane sensor. (b) Photograph of an as-fabricated flexible and transparent bionic membrane sensor. The scale bar is 1.0 cm. (c) A SEM image of surface-etched PTFE nanowires. The scale bar is 1  $\mu\text{m}$ . (d) The real-time voltage output when the sensors are placed over the carotid arteries of a 30-year-old man. The inset is an enlarged view of one cycle, which is a graphic representation of the augmentation index. (e) Quantitative comparison of the AIx and RI between the 30-year-old man and the 70-year-old man. (f) First-derivatives-of-the-pulse-waves (FDPWs) of a person under different activity states. Inset is the FDPWs of the four different participants. (g) Performance evaluation of the measured heartbeat profiles for biometric authentication. The variation of FAR and FRR in relation to the threshold indicates a low EER value of 3.5% at the threshold of  $7.3 \times 10^{-4}$ . Reproduced with permission from Wiley.

except that the vibration pattern of the PTFE tympanic membrane varied with different frequencies. The performance of the BMS as a

pressure sensor was comprehensively characterized, and a superior sensitivity of  $51 \text{ mV Pa}^{-1}$ , a rapid response time of 6 ms, a low detection limit of 2.5 Pa, and excellent stability over 40,000 cycles, which were comparable with the contact-mode self-powered pressure sensor demonstrated previously. As a live demonstration, a piece of 3 mg human air (13 Pa in contact pressure) was utilized to prove the low detection limit of the pressure sensor.

The BMS provided an outstanding route to obtain the human arterial pulse wave in a self-powered and noninvasive manner. It was attached onto the carotid, wrist, and chest for real time monitoring the arterial pulse, which induced a dynamic pressure change on the skin and could be characterized by the electrical output of the attached BMS. The recorded real-time voltage over several pulse periods for a 30-year-old man is shown in Fig. 20d, and the data was analyzed and compared with a 70-year-old man. Three clearly distinguishable determinants could be found in the characteristic pulse wave: Systolic peak ( $P_S$ ), point of inflection ( $P_I$ ), and diastolic wave ( $P_D$ ), which originated from the blood ejected from the left ventricle, the reflected pulse wave, and the ejected blood back to the left ventricle, respectively. Despite of the obvious difference in pulse wave profile, a more quantitative comparison was accomplished by two commonly used parameters: the augmentation index  $\text{AIx}(\%) = \pm(P_S - P_I)/PP$ , and the reflection index  $\text{RI} = h/\Delta t$ , where  $h$  is the subject height,  $\Delta t$  is the time delay between  $P_S$  and  $P_D$ , while  $PP$  is the absolute pulse wave magnitude. Based on the acquired waveforms, a statistical result of the AIx and RI was respectively obtained for the young and old man, as shown in Fig. 20e. For the younger man, average values of -30% and  $6.8 \text{ m s}^{-1}$  were respectively obtained for AIx and RI, while values of 24.8% and  $13.3 \text{ m s}^{-1}$  were obtained for the old man. The distinct difference in AIx and RI was mainly attributed to different arterial compliance capability between them. This difference could also be recognized through current measurement of the RMS. Meanwhile, the BMS could be attached to various body locations to obtain detailed information for cardiovascular risk estimation.

In addition, the BMS could also serve as a self-powered throat-attached microphone for voice recording and biometric identification. Its voice recording capability was realized by analyzing the Fourier spectrum of the measured output voltage, and high frequency signals could be filtered from the mixed message to recover the speaking content, which was a substantial progress than the previous work. In terms of biometric recognition, four sets of arterial pulse wave patterns were obtained, and Euclidean Metric

(EM) was calculated to measure the difference among pulse waves. Figure 20f shows the First-derivatives-of-the-pulse-waves (FDPWs) of the same person under different activity states, and its corresponding EMs were measured and compared with other individuals. It was discovered that the EM values of the FDPWs among different individuals were significantly larger than that for the same person under different activity states. Therefore, the distinguishable EMs of FDPWs could be used as the feature representation of pulse wave, acting as a threshold to separate the genuine pulse waves from the impostor ones, if an authentication system is established using pulse wave. The evaluation of this identification system was carried out among 120 randomly selected individuals, with 60 client patterns and 60 impostor patterns, respectively. The variation of its FAR and FRR in relation to the threshold is shown in Fig. 20g, and the intersection of the two curves at a certain threshold value of  $7.3 \times 10^{-4}$  indicated a low EER of 3.5%. On the basis of the numerous advantages of the BMS including self-powered, lightweight, simplicity in device fabrication, and outstanding reliability, the justified concepts and demonstrations in this work could be extensively adopted in wearable medical/health monitoring as well as biometric authentication, and came into effect of improving our living style.

To summarize, TENGs were widely and successfully adopted as self-powered active sensors (at least for the sensor tip part) under various circumstances, featured as being cost-effective, easy fabrication, environmentally friendly. The device performance correlates with many variables including the characteristics of applied forces (e.g. frequency, magnitude), environmental conditions (e.g. temperature, humidity) and also materials stability, which also renders certain challenge to the reliability of TENGs as self-powered active sensors. Since the contact between two materials may be difficult to be precisely controlled especially in the contact-separation mode once the applied force/pressure is large, quantification of the output signal may be inaccurate if the mechanical triggering exceeds a threshold value. But for smaller mechanical stimulation, TENG can be a reliable and sensitive choice.

## 7. TENG as a new technology for blue energy

Oceanic waves convey one of the most abundant energy sources on earth, with superior advantages over other energy sources including high volume, large scale, and much less dependence on weather, sunlight, and temperature conditions. However, this type of kinetic

energy has rarely been exploited due to lack of proper energy scavenging technologies. Since the invention and fast development of triboelectric nanogenerators as a new energy technology, a lot of efforts have been devoted to exploring approaches for effectively collecting various types of water-based power sources, namely blue energy harvesting. Up to now, several unique prototypes have been developed to achieve high output power, low cost, convenient

fabrication, good flexibility, excellent stability and robustness, and possibility to scale up, as summarized in Fig. 21. Despite the state-of-art progress, more endeavors are still highly desired to further investigate in this field to improve the performance of the water-TENG towards practical applications in blue energy harvesting.

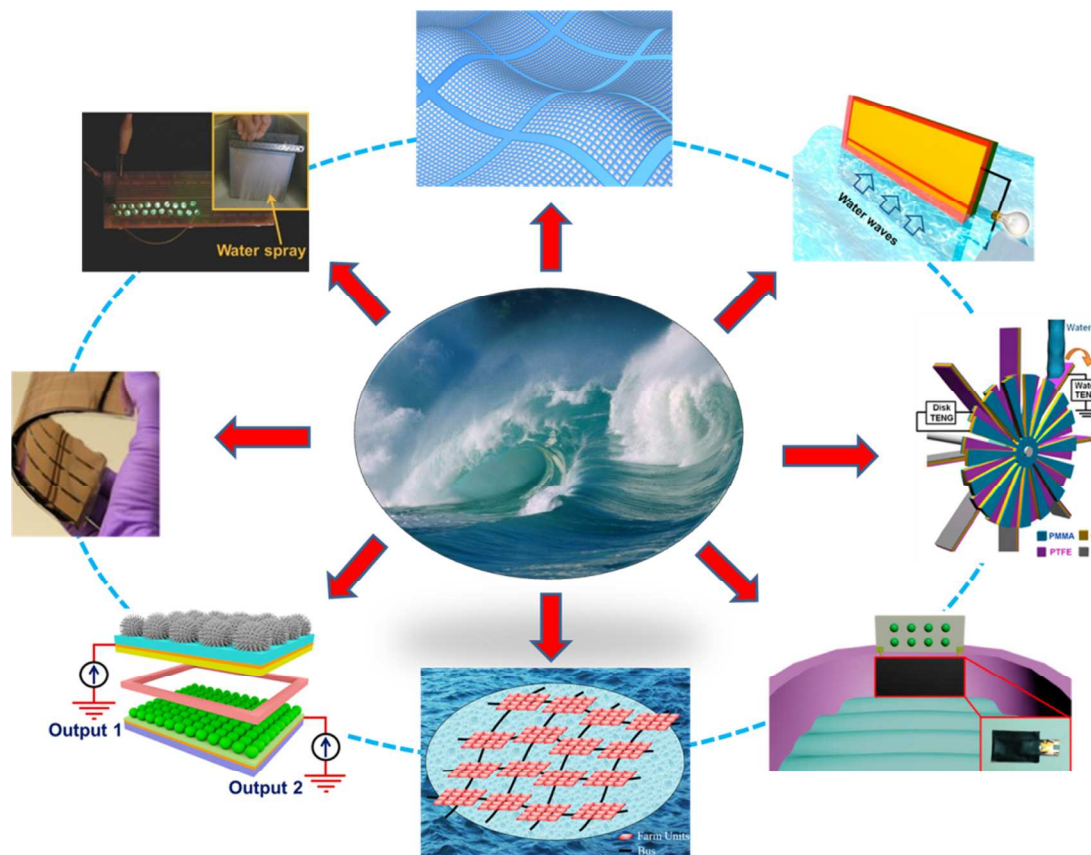


**Fig. 21** A schematic diagram exhibiting the state-of-art progress of TENGs for harvesting blue energy.

### 7.1 TENGs for harvesting water wave energy

The first design of blue energy harvester was raised by Lin *et al.* in 2013, when the concept water-solid contact electrification was first employed for energy harvesting in this work.<sup>134</sup> The device structure of this water-TENG is schematically illustrated in Fig. 22a, in which one dielectric layer of a typical contact-mode TENG was replaced with water. The cyclic contact between the PDMS layer and water surface would generate negative charges on PDMS layer and positive charges on water surface, and the periodical separation of the two charged surfaces resulted in change of potential difference between the two copper electrodes in the OC condition, and external electrons flow in the SC condition. Micropatterned pyramid array was created on the inner surface of the PDMS layer to enhance the

effective contact area (Fig. 22b), and this approach should be extraordinarily applicable in this case owing to high ductility of water. Driven by a linear motor at a frequency of 2 Hz and magnitude of 1.5 cm, the water-TENG was enabled to produce a  $V_{OC}$  and  $J_{SC}$  of 82 V and  $1.05 \text{ mA m}^{-2}$ , respectively. The optimized output power density reached up to  $50 \text{ mW m}^{-2}$  at 5 Hz. The frequency response of the water-TENG was significantly different from that of the solid-material-based TENG, in that the movement of the PDMS film contacting and separating from water would generate a water wave, which would disturb the contact area with the PDMS film. Figure 22c-d shows the frequency response of the measured  $J_{SC}$  and  $V_{OC}$ , respectively. Both of them decreased first from 2 to 3 Hz and then increased with frequency from 3 to 5 Hz. On the contrary, for solid-material-based TENG, the  $J_{SC}$  would keep increasing with the

frequency and the  $V_{OC}$  would remain almost unchanged. The difference of frequency response implied a unique feature of the water-TENG. It was further demonstrated that the water-TENG could serve as a self-powered temperature and ethanol sensor, through real time measurement of its output performance.

Another basic prototype of water-TENG was based on asymmetric screening of the triboelectric charges on a nanostructured hydrophobic thin film surface, as exhibited in Fig. 22e.<sup>135</sup> Two parallel strip-shaped electrodes were deposited on one side of a FEP thin film, and they were separated with a fine gap in between. The other side of the FEP thin film was modified with nanowire structures for improving the effective contact area. The operation of the water-TENG relied on a repetitive emerging-submerging process with traveling water waves, in which the coupling between triboelectrification and electrostatic induction drove alternating flows of electrons between electrodes. Quantitative assessment of the output performance was also stimulated by a linear motor, and the generated  $V_{OC}$  and  $I_{SC}$  were 160 V and 3  $\mu$ A, respectively, with an optimum output power of 0.12 mW at a velocity of 0.5 m/s (Fig. 22f). Three extrinsic factors were systematically investigated to optimize the electric output of the water-TENG, including velocity of the relative movement, aspect ratio of the device, and ion concentration of the water body. By conducting a series of control experiments, it was concluded that a higher velocity, finer electrode features, and lower ion concentration are all favorable for the overall output performance, though further systematic investigations on the charge generation process were still desirable to provide deeper insights. To demonstrate the applicability of the water-TENG in real-world situations, an integrated TENG with a scaled-up design was further tested in a normal environment where energy from ambient water motions was harvested. The integrated water-TENG consisted of six strip shaped electrodes and a total of five basic units were formed by any pair of adjacent electrodes. The electric output of each pair was first rectified then constructively superimposed through a parallel connection. It was then inserted into a traveling wave created by a large container, or placed beneath a sprinkler head with sprayed water droplets. The generated output current from both cases is shown in Figs. 22g and h, respectively. It is worth noting that the rectified current from water droplets (Fig. 22h) showed almost continuous DC behavior, which was attributed to numerous droplets and the merging of the large number of current peaks.

In addition to the above two fundamental structural designs, a lot

of other prototypes were also proposed for high performance blue energy harvesting. A dual-mode TENG was fabricated based on superhydrophobic  $TiO_2$  layer and polymer thin films to collect both the electrostatic and mechanical energy from flowing water.<sup>136</sup> The working of the hybrid water-TENG in this work relied on the

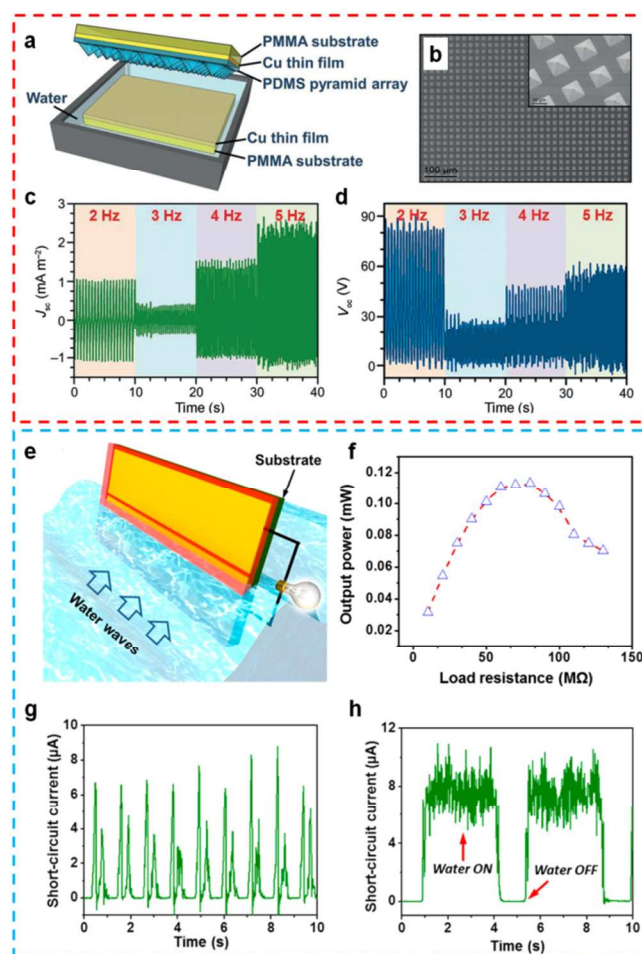


**Fig. 22** TENGs for harvesting water wave energy. (a) Schematic diagram of the water-TENG based on contact electrification between water and micro-patterned PDMS.<sup>134</sup> (b) SEM image of patterned PDMS pyramid array. Inset is an SEM image with higher magnification. (c-d) Influence of contact frequency between patterned PDMS pyramid array and deionized water on the (c)  $J_{SC}$  and (d)  $V_{OC}$  generated by the water-TENG. (e) Schematic of a substrate-supported TENG positioned in water waves. The up-and-down movement of the surrounding water body induces electricity generated between the two electrodes.<sup>135</sup> (f) Average output power of the water-TENG with increasing load resistance between electrodes. (g) Rectified short-circuit current of the integrated water-TENG when it interacts with water waves at a frequency of  $\sim 0.7$  Hz. (h) Rectified short-circuit current of the integrated water-TENG when it interacts with falling water drops.

Reproduced with permission from Wiley and American Chemical Society.

coupling of contact-separation and single-electrode operation mode. The generated  $I_{SC}$  from the two output terminals were 43 and 18  $\mu\text{A}$ , corresponding to output power densities of 1.31 and 0.38  $\text{W m}^{-2}$ , respectively.

A similar approach was also developed that employed the mechanical energy of water to drive a rotary-disk TENG.<sup>137</sup> Lin *et al.* continued to develop the water-TENG for harvesting raindrop energy, and two possible working mechanisms were proposed.<sup>138</sup> A broadband TENG based on wave-structured Kapton film was fabricated to harvest water wave energy with improved robustness, and this prototype could be integrated with the multi-strip-electrode structure to power up a distress signal emitter.<sup>139</sup> Hydropower harvesting could also be realized by a multilayered disk TENG integrated with a miniaturized turbine, while no water-solid electrification was involved in this work.<sup>53</sup>

Most recently, an innovative design was proposed by Chen and the co-workers to connect multiple TENG units into a network for large scale blue energy harvesting.<sup>140</sup> The TENG networks (TENG-NW) that naturally float on the water surface convert the slow, random, and high-force oscillatory wave energy into electricity, and an averaged power density of 1.15  $\text{MW km}^{-2}$  was predicted. Given the extremely low cost and unique applicability resulting from distinctive mechanism and simple structure, the TENG-NW renders a green alternative to traditional methods potentially for large-scale blue energy harvesting.

## 7.2 TENGs for harvesting wind energy

Besides water wave energy, wind energy is also a type of widely existed power source from the natural environment. Investigations on wind energy harvesting also plays a key role to overcome the limits of existing technologies. In this regard, a flutter-driven TENG was developed for effective wind energy harvesting to sustainably drive electronic devices in outdoor environments. The structure of the TENG in this work was composed of a fluttering flexible flag and a rigid plate, as shown in Fig. 23a.<sup>141</sup> The flag was a gold-coated conductive fabric that served as the fluttering body, and PTFE with counter electrode was attached onto the rigid plate to form a contact-mode TENG. Natural wind would introduce the contact-separation behavior of the flag and the rigid plate to generate electricity, and thus it was important to

understand the dynamic characteristics of flutters. As shown in Fig. 23b, a flexible woven flag exhibited oscillations with a node. From the top to the node, the oscillation amplitude was very small, but it was subject to increase as a travelling wave propagated toward the trailing edge below the node. To bring up a self-sustained contact-propagation-separation between two triboelectric layers through high frequency flag fluttering, the counter plate was simply placed next to the flag flutter within a critical distance, and the coupled interaction between the two surfaces was systematically investigated by varying their dimensions. The stability boundary could be characterized by a regime map shown in Fig. 23c, and two distinct contact-separation modes were observed in the plot. The transition from the single-contact mode in region A to the double-contact mode in region B occurred as the dimensionless mass decreased, which could be tuned by adjusting the length of the flag. Then, sequential images of the contact-propagation-separation behaviors for the single- and double-contact modes with different flag lengths were captured using a high-speed camera, and the details of the flag-plate interactions and transitions between different fluttering modes could be clearly identified. The flutter-driven TENG produced a high output of 200 V and 60  $\mu\text{A}$  at wind speed of 15  $\text{ms}^{-1}$ , with an average power density of 0.86  $\text{mW}$ . To demonstrate its wind energy harvesting capability in outdoor environments, a robust packaging module of the flutter-driven TENG was integrated (Fig. 23d) and securely mounted onto the roof of a moving vehicle. The TENG was enabled to charge a 1000  $\mu\text{F}$  capacitor to 30 V in 25 min when the vehicle was traveling at 70  $\text{km h}^{-1}$  (Fig. 23e), thus demonstrating its operation in an open environment under various wind conditions. A rotary TENG was also developed to harvest wind energy assisted by the wind-driven rotation of cup vanes, as shown in Fig. 23f.<sup>52</sup> The continuous shaft rotation introduced cyclic contact and consecutive sliding between Al foils and nanostructured PTFE film (Fig. 23g-h). Hence, the working principle of this rotary TENG relied on coupling of vertical contact-separation and lateral sliding modes. With a wind speed of  $\sim 15 \text{ m s}^{-1}$ , its  $V_{OC}$  and  $I_{SC}$  were up to 250 V and 0.25 mA, respectively, corresponding to a maximum power density of  $\sim 39 \text{ W m}^{-2}$ . Additionally, the rotary TENG could serve as a self-powered wind speed sensor (Fig. 23i-j). As expected, the  $I_{SC}$  increased drastically with rising wind speeds; but the  $V_{OC}$  also showed slight elevation as the wind speed went up. This result could be explained by the change in the surface charge density. With higher wind speed, the polymer thin films would obtain higher rotational torque and thus a larger contacting force, which led to

more intimate contact between two surfaces, resulting in a higher surface charge density. This invention may introduce a novel operation mechanism for wind generators and create a new

development area of the wind power using nanostructured surfaces of conventional materials.

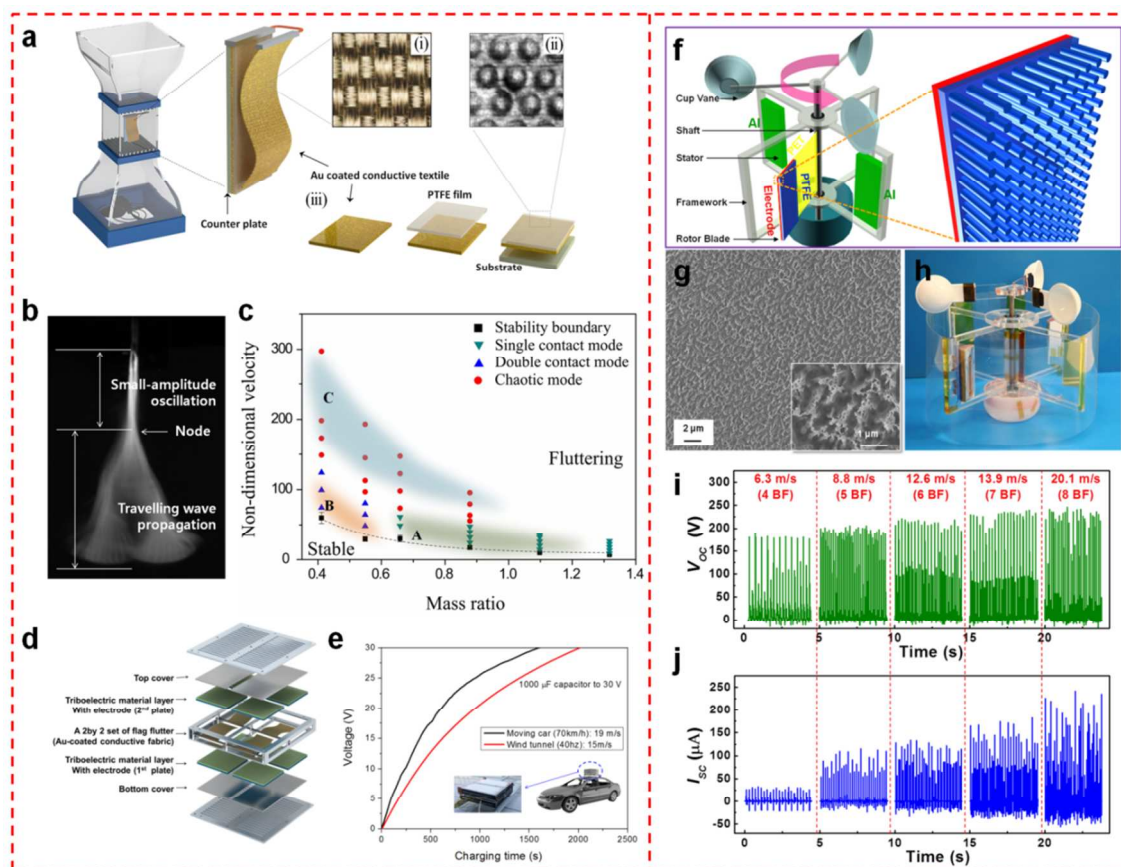


**Fig. 23** TENGs for harvesting the ambient wind energy. (a) Schematic diagrams of a wind tunnel and the structural design of a flutter-driven triboelectric generator including surface characteristics of (i) a highly flexible flag and (ii) a counter plate and (iii) the fabrication of the counter plate.<sup>141</sup> (b) Fluttering images of a stand-alone configuration of dimensions  $7.5 \times 5$  cm as captured with a high-speed camera. (c) The regime map of the dynamic interaction between a flag and a plate. (d) Schematic of the stacked TENG-packaging module with total eight units. (e) Comparison of the charging times of a 1,000- $\mu$ F capacitor using a stacked flutter-driven TENG system when charging on the moving vehicle and when charging in the wind tunnel system. (f) The schematic diagram showing the structural design of the rotary TENG, with the enlarged picture showing the nanowire structures on the surface of PTFE.<sup>52</sup> (g) The SEM image of the PTFE surface with etched nanowire structures. The inset is an SEM image at high magnification. (h) A photograph of the fabricated rotary TENG. (d-e) Influence of the wind speed on the electrical outputs. (d) The  $V_{OC}$  and (e) the  $I_{SC}$  under different wind speeds from 6.3 m/s (4 BF) to 20.1 m/s (8 BF). Reproduced with permission from Nature Publishing Group and American Chemical Society.

## 8. Summary and perspectives

As human beings are marching into the century of seeking for intelligent life and intelligent city, devices with high functionality are the fundamental components. A bottle neck for the sustainable operation of these devices is the electric power, although the power level for each is small but the number of units can be huge. Searching for self-powered system is a major drive in the field of nano energy. TENG has been an exciting technology because of its

high performance, high efficiency, low-cost, easy fabrication, diverse choices of materials, and easy scalability. Ever since its first invention in 2012,<sup>19</sup> TENG's instantaneous energy efficiency has reached 70%<sup>21</sup> and total energy conversion efficiency reached 85%.<sup>22</sup> TENG is being studied actively by over 50 research groups around the world.

Table 1 is a summary of the performance of the TENGs acting as various kinds of energy harvesters and self-powered active

sensors. It is like to be a feasible and most effective choice for building self-powered system to drive mobile electronics, sensor networks, flexible electronics and wearable electronics. With the introduction of new materials and surface engineering technologies, the efficiency of the TENG and overall system performance are expected to be significantly improved. We anticipate its outstanding impact to health monitoring, medical care, environmental protection, infrastructure monitoring and security.

**Table 1 A Summary of the Performance of TENGs as Sustainable Power Sources and Active Sensors.**

Power Sources		Active Sensors	
Mechanical Motions	$P_{\max}$	Sensing Objects	$S_{\max}$ or $R_{\max}$
Vibration	$104.6 \text{ W}\cdot\text{m}^{-2}$	Pressure Sensor	$44 \text{ mV}\cdot\text{Pa}^{-1}$
Rotation	$267 \text{ mW}\cdot\text{cm}^{-2}$	Vibration	$3.5 \mu\text{m}$
Linear Sliding	$50 \text{ mW}\cdot\text{cm}^{-2}$	Acoustic Sensor	$9.54 \text{ V}\cdot\text{Pa}^{-1}$
Finger Typing	$3.56 \text{ mW}\cdot\text{cm}^{-2}$	Displacement sensor	$173 \text{ nm}$
Blue Energy	$1.15 \text{ MW}\cdot\text{Km}^{-2}$	Acceleration sensor	$15.56 \text{ V}\cdot\text{g}^{-1}$
Wind Energy	$39 \text{ W}\cdot\text{m}^{-2}$	Hg <sup>2+</sup> ions	$30 \text{ nM}$
Acoustic Energy	$121 \text{ mW}\cdot\text{m}^{-2}$	Phenol	$0.01 \mu\text{M}^{-1}$

$P_{\max}$ ,  $S_{\max}$  and  $R_{\max}$  denotes the reported highest power density, sensitivity and resolution reported by June 2015, respectively.

TENG can be a high sensitive self-powered sensor for detecting mechanical triggering, stimulation and movement. The electric current and voltage signals generated by TENG represent the dynamic and static information, respectively, regarding a mechanical action. Such sensor tip does not need a power to drive it, which is a major difference in comparison to conventional sensors. Applications can be found in areas of micromechanical systems, human-machine interfacing, touch-pad technology, security systems and motion sensing.

In recent years, TENGs have shown tremendous achievements in both fundamental understanding and technological improvements. As toward the future applications of TENGs, certain main issues and problems needs to be addressed:

- (1) Understanding the fundamental mechanism of contact electrification. This phenomenon has been studied for a long time, and a few models have been established to explain the charge generation process, but no substantial conclusion has been reached. It will be of great importance to understand the charge transfer process to optimize the performance of the TENGs.
- (2) Establishing a standard to calibrate the performance of a TENG. Four fundamental modes have been invented for TENG, each of which has specific design and choice of materials. Establishing standards for comparing and calibrating the performance of TENG is critical. Recently, Zi et al.<sup>142</sup> has established such criteria. As for

materials, the surface charge density is a sole measure of the performance's performance for TENG.

- (3) Developing effective packaging technology for TENGs. The packaging of TENGs will be vitally important to make it a commercialized products especially for application in variety of harsh environment, because moisture or any surface contaminants can largely affect the performance of the TENG. However, packaging of TENGs may be more difficult than that of traditional MEMS devices,

since TENGs contain parts in motion and possible air gaps to separate surface charges.

- (4) Find a suitable approach for power management. One advantage of TENG is its high open-circuit voltage, while its short-circuit current is usually lower than that of solar cells or thermoelectric cells. It is targeted to harvest "random" and possibly low-frequency mechanical signals. As for such cases, the traditional transformer produces a lot loss in the power management. Hence, a power management approach is desirable to reduce its output voltage and boost its output current at the minimized power loss.

- (5) Improving device durability and output stability. This is always a vital issue for TENG especially in comparison to the traditional generator based on electromagnetic induction. New materials and coupled modes of operations would be good choices.

- (6) Integrating TENG with a sensor to form a self-powered system with considering the practical environment in which the system will be employed.

- (7) ...

Figure 24 presents the "tree" idea of our approach regarding the development of nanogenerators (left-hand half).<sup>143</sup> Starting from fundamental materials and physics effects, tiny mechanical energy can be effectively converted into electricity using nanogenerators, which can be a fundamental approach for intelligent earth with applications in internet of things, mobile/wearable electronics, fabric

electronics, environmental protection, health care, infrastructure monitoring, and national security.

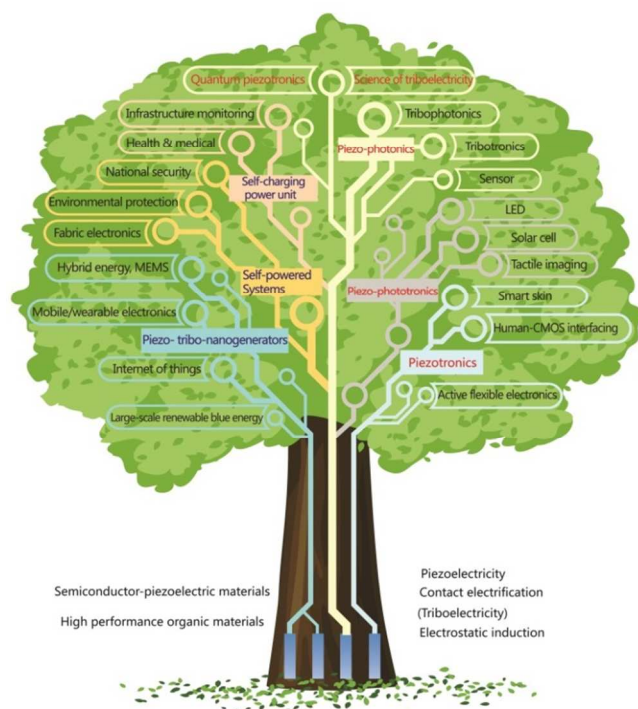


**Fig. 24** A tree-design schematic represented blue print about the nanogenerator driven self-powered systems and piezotronics led sensors and energy sciences.<sup>142</sup> It should be noted that the content in this review covered the left branches of the tree-design. Reproduced with permission from Elsevier.

TENG has the potential to be a new approach for harvesting ocean wave energy, although this is a long term goal. It could be a revolutionary technology in comparison to the classical electromechanical generator with complementary areas of applications. We hope the dream of blue energy could be realized in some day, so that human will have endless power supplied by nature.

**Acknowledgement.** Research was supported by DOE, NSF, MANA NIMS (Japan), the Knowledge Innovation Program of the Chinese Academy of Sciences (KJCX2-YW-M13), the Hightower Chair foundation, and the "thousands talents" program for pioneer researcher and his innovation team, China. We thank my group members and our collaborators for their contributions to the work reviewed here, especially to those ones: Fengru Fan, Guang Zhu, Sihong Wang, Ya Yang, Zong-Hong Lin, Yusheng Zhou, Simiao Niu, Jin Yang, Weiqing Yang, Xiaonan Wen, Xia Cao, Jun Zhou, Yong Qin, Xing Fan, Gang Cheng, Li Zheng, Yunlong Zi, Chi

Zhang, Changbao Han, Wei Tang, Aifang Yu, Hulin Zhang, Yannan Xie, Peng Bai, Qingshen Jing, Yuanjie Su, Min-Hsin Yeh, Fang Yi, Zhaoling Li, Hengyu Guo, Zhen Wen, Caofeng Pan, Ying Liu, Te-Chien Hou, Po-Kang Yang, Yue Zhang, Zhong-Qun Tian, Tao Zhou, Mengxiao Chen, Limin Zhang, and Weiming Du.

## Notes and References

<sup>a</sup> School of Materials Science and Engineering, Georgia Institute of Technology, Atlanta, Georgia 30332-0245, United States. E-mail: zlwang@gatech.edu

<sup>b</sup> Beijing Institute of Nanoenergy and Nanosystems, Chinese Academy of Sciences, Beijing, 100083, China.

†Electronic Supplementary Information (ESI) available. See DOI: 10.1039/b000000x/

‡Jun Chen and Long Lin made equal contribution to this review.

- 1 D. Evans, *Cisco IBSG*, 2011.
- 2 Z. L. Wang, *Sci. Am.*, 2008, **298**, 82-87.
- 3 Z. L. Wang and J. Song, *Science*, 2006, **312**, 242-246.
- 4 Y. Gao and Z. L. Wang, *Nano Lett.*, 2007, **7**, 2499-2505.
- 5 Y. Qin, X. Wang and Z. L. Wang, *Nature*, 2008, **451**, 809-813.
- 6 X. Wang, J. Song, J. Liu and Z. L. Wang, *Science*, 2007, **316**, 102-105.
- 7 S. Xu, B. J. Hansen and Z. L. Wang, *Nat. Commun.*, 2010, **1**, 93.
- 8 S. Xu, Y. Qin, C. Xu, Y. Wei, R. Yang, Z. L. Wang, *Nat. Nanotechnol.*, 2010, **5**, 366-373.
- 9 R. Yang, Y. Qin, L. Dai, Z. L. Wang, *Nat. Nanotechnol.*, 2009, **4**, 34-39.
- 10 J. Henniker, *Nature*, 1962, **196**, 474-474.
- 11 R. G. Horn and D. T. Smith, *Science*, 1992, **256**, 362-364.
- 12 R. G. Horn, D. T. Smith and A. Grabbe, *Nature*, 1993, **366**, 442-443.
- 13 Z. L. Wang, *Adv. Funct. Mater.*, 2008, **18**, 3553-3567.
- 14 Z. L. Wang, *Mater. Sci. and Eng. Reports*, 2009, **64**, 33-71.
- 15 Z. L. Wang, *Nanogenerators for Self-Powered Devices and Systems*, Georgia Institute of Technology, Georgia Institute of Technology, 2011.
- 16 Z. L. Wang, *Adv. Mater.*, 2012, **24**, 280-285.
- 17 Z. L. Wang and W. Wu, *Angew. Chem. Int. Ed.*, 2012, **51**, 11700-11721.
- 18 Z. L. Wang, G. Zhu, Y. Yang, S. Wang, C. Pan, *Mater. Today*, 2012, **15**, 532-543.
- 19 F.-R. Fan, Z.-Q. Tian and Z. L. Wang, *Nano Energy*, 2012, **1**, 328-334.
- 20 G. Zhu, Y. S. Zhou, P. Bai, X. S. Meng, Q. Jing, J. Chen and Z.L. Wang, *Adv. Mater.*, 2014, **26**, 3788-3796.
- 21 W. Tang, T. Jiang, F.R. Fan, A.F. Yu, C. Zhang, X. Cao, Z. L. Wang, *Adv. Funct. Mater.*, 2015, DOI: 10.1002/adfm.201501331.
- 22 Y. Xie, S. Wang, S. Niu, L. Lin, Q. Jing, J. Yang, Z. Wu and Z. L. Wang, *Adv. Mater.*, 2014, **26**, 6599-6607.
- 23 G. Zhu, B. Peng, J. Chen, Q. Jing and Z. Lin Wang, *Nano*

- Energy, 2015, DOI:10.1016/j.nanoen.2014.11.050.
- 24 S. Wang, L. Lin and Z. L. Wang, *Nano Energy*, 2015, **11**, 436-462.
- 25 Z. L. Wang, *Faraday Discuss.*, 2014, **176**, 447-458.
- 26 Z. L. Wang, *ACS Nano*, 2013, **7**, 9533-9557.
- 27 G. Zhu, C. Pan, W. Guo, C.-Y. Chen, Y. Zhou, R. Yu and Z. L. Wang, *Nano Lett.*, 2012, **12**, 4960-4965.
- 28 S. Wang, L. Lin and Z. L. Wang, *Nano Lett.*, 2012, **12**, 6339-6346.
- 29 F.-R. Fan, L. Lin, G. Zhu, W. Wu, R. Zhang and Z. L. Wang, *Nano Lett.*, 2012, **12**, 3109-3114.
- 30 G. Zhu, Z.-H. Lin, Q. Jing, P. Bai, C. Pan, Y. Yang, Y. Zhou and Z. L. Wang, *Nano Lett.*, 2013, **13**, 847-853.
- 31 J. Chen, G. Zhu, W. Yang, Q. Jing, P. Bai, Y. Yang, T.-C. Hou and Z. L. Wang, *Adv. Mater.*, 2013, **25**, 6094-6099.
- 32 P. Bai, G. Zhu, Z.-H. Lin, Q. Jing, J. Chen, G. Zhang, J. Ma and Z. L. Wang, *ACS Nano*, 2013, **7**, 3713-3719.
- 33 G. Zhu, P. Bai, J. Chen and Z. L. Wang, *Nano Energy*, 2013, **2**, 688-692.
- 34 W. Yang, J. Chen, G. Zhu, X. Wen, P. Bai, Y. Su, Y. Lin and Z. L. Wang, *Nano Res.*, 2013, **6**, 880-886.
- 35 J. Zhong, Q. Zhong, F. Fan, Y. Zhang, S. Wang, B. Hu, Z. L. Wang and J. Zhou, *Nano Energy*, 2013, **2**, 491-497.
- 36 W. Yang, J. Chen, G. Zhu, J. Yang, P. Bai, Y. Su, Q. Jing, X. Cao and Z. L. Wang, *ACS Nano*, 2013, **7**, 11317-11324.
- 37 T.-C. Hou, Y. Yang, H. Zhang, J. Chen, L.-J. Chen and Z. L. Wang, *Nano Energy*, 2013, **2**, 856-862.
- 38 X.-S. Zhang, M.-D. Han, R.-X. Wang, F.-Y. Zhu, Z.-H. Li, W. Wang and H.-X. Zhang, *Nano Lett.*, 2013, **13**, 1168-1172.
- 39 Y. Yang, L. Lin, Y. Zhang, Q. Jing, T.-C. Hou and Z. L. Wang, *ACS Nano*, 2012, **6**, 10378-10383.
- 40 L. Lin, Y. Xie, S. Wang, W. Wu, S. Niu, X. Wen and Z. L. Wang, *ACS Nano*, 2013, **7**, 8266-8274.
- 41 Z.-H. Lin, G. Zhu, Y. S. Zhou, Y. Yang, P. Bai, J. Chen and Z. L. Wang, *Angew. Chem. Int. Ed.*, 2013, **52**, 5065-5069.
- 42 Z.-H. Lin, Y. Xie, Y. Yang, S. Wang, G. Zhu and Z. L. Wang, *ACS Nano*, 2013, **7**, 4554-4560.
- 43 X. Fan, J. Chen, J. Yang, P. Bai, Z. Li and Z. L. Wang, *ACS Nano*, 2015, **9**, 4236-4243.
- 44 J. Yang, J. Chen, Y. Liu, W. Yang, Y. Su and Z. L. Wang, *ACS Nano*, 2014, **8**, 2649-2657.
- 45 G. Zhu, J. Chen, Y. Liu, P. Bai, Y. S. Zhou, Q. Jing, C. Pan and Z. L. Wang, *Nano Lett.*, 2013, **13**, 2282-2289.
- 46 S. Wang, L. Lin, Y. Xie, Q. Jing, S. Niu and Z. L. Wang, *Nano Lett.*, 2013, **13**, 2226-2233.
- 47 G. Zhu, J. Chen, T. Zhang, Q. Jing and Z. L. Wang, *Nat. Commun.*, 2014, **5**, 3426.
- 48 Q. Jing, G. Zhu, P. Bai, Y. Xie, J. Chen, R. P. S. Han and Z. L. Wang, *ACS Nano*, 2014, **8**, 3836-3842.
- 49 L. Lin, S. Wang, Y. Xie, Q. Jing, S. Niu, Y. Hu and Z. L. Wang, *Nano Lett.*, 2013, **13**, 2916-2923.
- 50 C. Zhang, T. Zhou, W. Tang, C. Han, L. Zhang and Z. L. Wang, *Adv. Energy Mater.*, 2014, **4**, 1301798.
- 51 P. Bai, G. Zhu, Y. Liu, J. Chen, Q. Jing, W. Yang, J. Ma, G. Zhang and Z. L. Wang, *ACS Nano*, 2013, **7**, 6361-6366.
- 52 Y. Xie, S. Wang, L. Lin, Q. Jing, Z.-H. Lin, S. Niu, Z. Wu and Z. L. Wang, *ACS Nano*, 2013, **7**, 7119-7125.
- 53 Y. Xie, S. Wang, S. Niu, L. Lin, Q. Jing, Y. Su, Z. Wu and Z. L. Wang, *Nano Energy*, 2014, **6**, 129-136.
- 54 Y. S. Zhou, G. Zhu, S. Niu, Y. Liu, P. Bai, Q. Jing and Z. L. Wang, *Adv. Mater.*, 2014, **26**, 1719-1724.
- 55 Q. Jing, G. Zhu, W. Wu, P. Bai, Y. Xie, R. P. S. Han and Z. L. Wang, *Nano Energy*, 2014, **10**, 305-312.
- 56 Y. Yang, H. Zhang, J. Chen, Q. Jing, Y. S. Zhou, X. Wen and Z. L. Wang, *ACS Nano*, 2013, **7**, 7342-7351.
- 57 S. Niu, Y. Liu, S. Wang, L. Lin, Y. S. Zhou, Y. Hu and Z. L. Wang, *Adv. Funct. Mater.*, 2014, **24**, 3332-3340.
- 58 Y. Yang, G. Zhu, H. Zhang, J. Chen, X. Zhong, Z.-H. Lin, Y. Su, P. Bai, X. Wen and Z. L. Wang, *ACS Nano*, 2013, **7**, 9461-9468.
- 59 H. Zhang, Y. Yang, X. Zhong, Y. Su, Y. Zhou, C. Hu and Z. L. Wang, *ACS Nano*, 2014, **8**, 680-689.
- 60 Q. Liang, X. Yan, Y. Gu, K. Zhang, M. Liang, S. Lu, X. Zheng and Y. Zhang, *Sci. Rep.*, 2015, **5**, 9080.
- 61 Q. Zhong, J. Zhong, B. Hu, Q. Hu, J. Zhou and Z. L. Wang, *Energy Environ. Sci.*, 2013, **6**, 1779-1784.
- 62 B. Meng, W. Tang, Z.-H. Too, X. Zhang, M. Han, W. Liu and H. Zhang, *Energy Environ. Sci.*, 2013, **6**, 3235-3240.
- 63 Y. Yang, H. Zhang, Z.-H. Lin, Y. S. Zhou, Q. Jing, Y. Su, J. Yang, J. Chen, C. Hu and Z. L. Wang, *ACS Nano*, 2013, **7**, 9213-9222.
- 64 G. Zhu, W. Q. Yang, T. Zhang, Q. Jing, J. Chen, Y. S. Zhou, P. Bai and Z. L. Wang, *Nano Lett.*, 2014, **14**, 3208-3213.
- 65 F. Yi, L. Lin, S. Niu, J. Yang, W. Wu, S. Wang, Q. Liao, Y. Zhang and Z. L. Wang, *Adv. Funct. Mater.*, 2014, **24**, 7488-7494.
- 66 Y. Su, G. Zhu, W. Yang, J. Yang, J. Chen, Q. Jing, Z. Wu, Y. Jiang and Z. L. Wang, *ACS Nano*, 2014, **8**, 3843-3850.
- 67 Y. Wu, Q. Jing, J. Chen, P. Bai, J. Bai, G. Zhu, Y. Su and Z. L. Wang, *Adv. Funct. Mater.*, 2015, **25**, 2166-2174.
- 68 H. Zhang, Y. Yang, Y. Su, J. Chen, K. Adams, S. Lee, C. Hu and Z. L. Wang, *Adv. Funct. Mater.*, 2014, **24**, 1401-1407.
- 69 H. Zhang, Y. Yang, T.-C. Hou, Y. Su, C. Hu and Z. L. Wang, *Nano Energy*, 2013, **2**, 1019-1024.
- 70 H. Zhang, Y. Yang, Y. Su, J. Chen, C. Hu, Z. Wu, Y. Liu, C. P. Wong, Y. Bando and Z. L. Wang, *Nano Energy*, 2013, **2**, 693-701.
- 71 P.-K. Yang, Z.-H. Lin, K. C. Pradel, L. Lin, X. Li, X. Wen, J.-H. He and Z. L. Wang, *ACS Nano*, 2015, **9**, 901-907.
- 72 P. Bai, G. Zhu, Q. Jing, J. Yang, J. Chen, Y. Su, J. Ma, G. Zhang and Z. L. Wang, *Adv. Funct. Mater.*, 2014, **24**, 5807-5813.
- 73 F. Yi, L. Lin, S. Niu, P.-K. Yang, Z. Wang, J. Chen, Y. Zhou, Y. Zi, J. Wang, Q. Liao, Y. Zhang and Z. L. Wang, *Adv. Funct. Mater.*, 2015, DOI: 10.1002/adfm.201500428.
- 74 W. Yang, J. Chen, X. Wen, Q. Jing, J. Yang, Y. Su, G. Zhu, W. Wu and Z. L. Wang, *ACS Appl. Mater. Interfaces*, 2014, **6**, 7479-7484.
- 75 P. Bai, G. Zhu, Q. Jing, Y. Wu, J. Yang, J. Chen, J. Ma, G. Zhang and Z. L. Wang, *Nano Energy*, 2015, **12**, 278-286.
- 76 Y. Su, X. Wen, G. Zhu, J. Yang, J. Chen, P. Bai, Z. Wu, Y. Jiang and Z. L. Wang, *Nano Energy*, 2014, **9**, 186-195.
- 77 S. Wang, Y. Xie, S. Niu, L. Lin and Z. L. Wang, *Adv. Mater.*, 2014, **26**, 2818-2824.

- 78 L. Lin, Y. Xie, S. Niu, S. Wang, P.-K. Yang and Z. L. Wang, *ACS Nano*, 2015, **9**, 922-930.
- 79 S. Wang, S. Niu, J. Yang, L. Lin and Z. L. Wang, *ACS Nano*, 2014, **8**, 12004-12013.
- 80 H. Guo, J. Chen, M.-H. Yeh, X. Fan, Z. Wen, Z. Li, C. Hu and Z. L. Wang, *ACS Nano*, 2015, **9**, 5577-5584.
- 81 L. Lin, S. Wang, S. Niu, C. Liu, Y. Xie and Z. L. Wang, *ACS Appl. Mater. Interfaces*, 2014, **6**, 3031-3038.
- 82 H. Guo, Q. Leng, X. He, M. Wang, J. Chen, C. Hu and Y. Xi, *Adv. Energy Mater.*, 2015, **5**, 1400790.
- 83 H. Guo, X. He, J. Zhong, Q. Zhong, Q. Leng, C. Hu, J. Chen, L. Tian, Y. Xi and J. Zhou, *J. Mater. Chem. A*, 2014, **2**, 2079-2087.
- 84 C. Zhang, W. Tang, Y. Pang, C. Han and Z. L. Wang, *Adv. Mater.*, 2015, **27**, 719-726.
- 85 S. Niu, S. Wang, L. Lin, Y. Liu, Y. S. Zhou, Y. Hu and Z. L. Wang, *Energy Environ. Sci.*, 2013, **6**, 3576-3583.
- 86 S. Niu, Y. Liu, S. Wang, L. Lin, Y. S. Zhou, Y. Hu and Z. L. Wang, *Adv. Mater.*, 2013, **25**, 6184-6193.
- 87 S. Niu, Y. Liu, X. Chen, S. Wang, Y. S. Zhou, L. Lin, Y. Xie and Z. L. Wang, *Nano Energy*, 2015, **12**, 760-774.
- 88 S. Niu, S. Wang, Y. Liu, Y. S. Zhou, L. Lin, Y. Hu, K. C. Pradel and Z. L. Wang, *Energy Environ. Sci.*, 2014, **7**, 2339-2349.
- 89 S. Niu, Y. Liu, Y. S. Zhou, S. Wang, L. Lin and Z. L. Wang, *IEEE Trans. Electron Devices*, 2015, **62**, 641-647.
- 90 S. Niu and Z. L. Wang, *Nano Energy*, 2015, DOI:10.1016/j.nanoen.2014.11.034.
- 91 Y. S. Zhou, S. Wang, Y. Yang, G. Zhu, S. Niu, Z.-H. Lin, Y. Liu and Z. L. Wang, *Nano Lett.*, 2014, **14**, 1567-1572.
- 92 S. Wang, Y. Xie, S. Niu, L. Lin, C. Liu, Y. S. Zhou and Z. L. Wang, *Adv. Mater.*, 2014, **26**, 6720-6728.
- 93 Z. Wang, L. Cheng, Y. Zheng, Y. Qin and Z. L. Wang, *Nano Energy*, 2014, **10**, 37-43.
- 94 S.-H. Shin, Y. H. Kwon, Y.-H. Kim, J.-Y. Jung, M. H. Lee and J. Nah, *ACS Nano*, 2015, **9**, 4621-4627.
- 95 C. K. Jeong, K. M. Baek, S. Niu, T. W. Nam, Y. H. Hur, D. Y. Park, G.-T. Hwang, M. Byun, Z. L. Wang, Y. S. Jung and K. J. Lee, *Nano Lett.*, 2014, **14**, 7031-7038.
- 96 W. Yang, J. Chen, Q. Jing, J. Yang, X. Wen, Y. Su, G. Zhu, P. Bai and Z. L. Wang, *Adv. Funct. Mater.*, 2014, **24**, 4090-4096.
- 97 W. Du, X. Han, L. Lin, M. Chen, X. Li, C. Pan and Z. L. Wang, *Adv. Energy Mater.*, 2014, **4**, 1301592.
- 98 W. Tang, C. Zhang, C. B. Han and Z. L. Wang, *Adv. Funct. Mater.*, 2014, **24**, 6684-6690.
- 99 S. Wang, Z.-H. Lin, S. Niu, L. Lin, Y. Xie, K. C. Pradel and Z. L. Wang, *ACS Nano*, 2013, **7**, 11263-11271.
- 100 X. Pu, L. Li, H. Song, C. Du, Z. Zhao, C. Jiang, G. Cao, W. Hu and Z. L. Wang, *Adv. Mater.*, 2015, **27**, 2472-2478.
- 101 G. Cheng, L. Zheng, Z.-H. Lin, J. Yang, Z. Du and Z. L. Wang, *Adv. Energy Mater.*, 2015, **5**, 1401452.
- 102 C. Xu, X. Wang and Z. L. Wang, *J. Am. Chem. Soc.*, 2009, **131**, 5866-5872.
- 103 C. Xu and Z. L. Wang, *Adv. Mater.*, 2011, **23**, 873-877.
- 104 Y. Wu, X. Zhong, X. Wang, Y. Yang and Z. Wang, *Nano Res.*, 2014, **7**, 1631-1639.
- 105 Y. Yang, H. Zhang, G. Zhu, S. Lee, Z.-H. Lin and Z. L. Wang, *ACS Nano*, 2013, **7**, 785-790.
- 106 L. Zheng, Z.-H. Lin, G. Cheng, W. Wu, X. Wen, S. Lee and Z. L. Wang, *Nano Energy*, 2014, **9**, 291-300.
- 107 Y. Hu, J. Yang, S. Niu, W. Wu and Z. L. Wang, *ACS Nano*, 2014, **8**, 7442-7450.
- 108 X. Wang, S. Wang, Y. Yang and Z. L. Wang, *ACS Nano*, 2015, **9**, 4553-4562.
- 109 Y. Yang, H. Zhang, Z.-H. Lin, Y. Liu, J. Chen, Z. Lin, Y. S. Zhou, C. P. Wong and Z. L. Wang, *Energy Environ. Sci.*, 2013, **6**, 2429-2434.
- 110 Y. Yang, H. Zhang, J. Chen, S. Lee, T.-C. Hou and Z. L. Wang, *Energy Environ. Sci.*, 2013, **6**, 1744-1749.
- 111 C. Zhang, W. Tang, C. Han, F. Fan and Z. L. Wang, *Adv. Mater.*, 2014, **26**, 3580-3591.
- 112 F.-R. Fan, W. Tang, Y. Yao, J. Luo, C. Zhang and Z. L. Wang, *Nanotechnology*, 2014, **25**, 135402.
- 113 Y. Yang, H. Zhang, S. Lee, D. Kim, W. Hwang and Z. L. Wang, *Nano Lett.*, 2013, **13**, 803-808.
- 114 Y. Zi, L. Lin, J. Wang, S. Wang, J. Chen, X. Fan, P.-K. Yang, F. Yi and Z. L. Wang, *Adv. Mater.*, 2015, **27**, 2340-2347.
- 115 P. Bai, G. Zhu, Y. Zhou, S. Wang, J. Ma, G. Zhang and Z. Wang, *Nano Res.*, 2014, **7**, 990-997.
- 116 M. Han, X.-S. Zhang, B. Meng, W. Liu, W. Tang, X. Sun, W. Wang and H. Zhang, *ACS Nano*, 2013, **7**, 8554-8560.
- 117 X. Li, Z.-H. Lin, G. Cheng, X. Wen, Y. Liu, S. Niu and Z. L. Wang, *ACS Nano*, 2014, **8**, 10674-10681.
- 118 Y. Yang, H. Zhang, Y. Liu, Z.-H. Lin, S. Lee, Z. Lin, C. P. Wong and Z. L. Wang, *ACS Nano*, 2013, **7**, 2808-2813.
- 119 L. Zheng, G. Cheng, J. Chen, L. Lin, J. Wang, Y. Liu and Z. L. Wang, *Adv. Energy Mater.*, 2015, under review.
- 120 Q. Zheng, B. Shi, F. Fan, X. Wang, L. Yan, W. Yuan, S. Wang, H. Liu, Z. Li and Z. L. Wang, *Adv. Mater.*, 2014, **26**, 5851-5856.
- 121 W. Tang, Y. Han, C. B. Han, C. Z. Gao, X. Cao and Z. L. Wang, *Adv. Mater.*, 2015, **27**, 272-276.
- 122 S. Chen, C. Gao, W. Tang, H. Zhu, Y. Han, Q. Jiang, T. Li, X. Cao and Z. L. Wang, *Nano Energy*, 2015, DOI:10.1016/j.nanoen.2014.12.013.
- 123 M.-H. Yeh, L. Lin, P.-K. Yang and Z. L. Wang, *ACS Nano*, 2015, **9**, 4757-4765.
- 124 Y. Yang, Y. S. Zhou, H. Zhang, Y. Liu, S. Lee and Z. L. Wang, *Adv. Mater.*, 2013, **25**, 6594-6601.
- 125 J. Luo, F. R. Fan, T. Zhou, W. Tang, F. Xue and Z. L. Wang, *Extrem. Mech. Lett.*, 2015, **2**, 28-36.
- 126 C. B. Han, C. Zhang, X. H. Li, L. Zhang, T. Zhou, W. Hu and Z. L. Wang, *Nano Energy*, 2014, **9**, 325-333.
- 127 Y. Hu, J. Yang, Q. Jing, S. Niu, W. Wu and Z. L. Wang, *ACS Nano*, 2013, **7**, 10424-10432.
- 128 J. Yang, J. Chen, Y. Yang, H. Zhang, W. Yang, P. Bai, Y. Su and Z. L. Wang, *Adv. Energy Mater.*, 2014, **4**, 1301322.
- 129 A. Yu, M. Song, Y. Zhang, Y. Zhang, L. Chen, J. Zhai, Z. L. Wang, *Nano Res.*, 2015, **8**, 765-773.
- 130 Z.-H. Lin, G. Cheng, Y. Yang, Y. S. Zhou, S. Lee and Z. L. Wang, *Adv. Funct. Mater.*, 2014, **24**, 2810-2816.
- 131 Z. Li, J. Chen, J. Yang, Y. Su, X. Fan, Y. Wu, C. Yu and Z. L. Wang, *Energy Environ. Sci.*, 2015, **8**, 887-896.
- 132 J. Chen, G. Zhu, J. Yang, Q. Jing, P. Bai, W. Yang, X. Qi, Y. Su and Z. L. Wang, *ACS Nano*, 2015, **9**, 105-116.

- 133 J. Yang, J. Chen, Y. Su, Q. Jing, Z. Li, F. Yi, X. Wen, Z. Wang and Z. L. Wang, *Adv. Mater.*, 2015, **27**, 1316-1326.
- 134 Z.-H. Lin, G. Cheng, L. Lin, S. Lee and Z. L. Wang, *Angew. Chem. Int. Ed.*, 2013, **125**, 12777-12781.
- 135 G. Zhu, Y. Su, P. Bai, J. Chen, Q. Jing, W. Yang and Z. L. Wang, *ACS Nano*, 2014, **8**, 6031-6037.
- 136 Z.-H. Lin, G. Cheng, W. Wu, K. C. Pradel and Z. L. Wang, *ACS Nano*, 2014, **8**, 6440-6448.
- 137 G. Cheng, Z.-H. Lin, Z. Du and Z. L. Wang, *ACS Nano*, 2014, **8**, 1932-1939.
- 138 Z.-H. Lin, G. Cheng, S. Lee, K. C. Pradel and Z. L. Wang, *Adv. Mater.*, 2014, **26**, 4690-4696.
- 139 X. Wen, W. Yang, Q. Jing and Z. L. Wang, *ACS Nano*, 2014, **8**, 7405-7412.
- 140 J. Chen, J. Yang, Z. Li, X. Fan, Y. Zi, Q. Jing, H. Guo, Z. Wen, K. C. Pradel, S. Niu and Z. L. Wang, *ACS Nano*, 2015, **9**, 3324-3331.
- 141 J. Bae, J. Lee, S. Kim, J. Ha, B.-S. Lee, Y. Park, C. Choong, J.-B. Kim, Z. L. Wang, H.-Y. Kim, J.-J. Park and U. I. Chung, *Nat. Commun.*, 2014, **5**, 4929.
- 142 Y.L. Zi, S.M. Niu, J. Wang, Z. Wen, W. Tang, Z. L. Wang, submitted.
- 143 Z. L. Wang and X. Wang, *Nano Energy*, 2015, Doi:10.1016/j.nanoen.2015.01.011.



**Dr. Zhong Lin (ZL) Wang** is the Hightower Chair in Materials Science and Engineering and Regents' Professor at Georgia Tech. He is also the chief scientist and director of the Beijing Institute of Nanoenergy and Nanosystems, Chinese Academy of Sciences. His discovery and breakthroughs in developing nanogenerators establish the principle and technological road map for harvesting mechanical energy from environment and biological systems for powering a personal electronics. His research on self-powered nanosystems has inspired the worldwide effort in academia and industry for studying energy for micro-nano-systems, which is now a distinct disciplinary in energy research and future sensor networks. Dr. Wang received 2014 World Technology Prize in Materials; 2014 the James C. McGroddy Prize for New Materials from America Physical Society, 2013 ACS Nano Lectureship award, 2012 Edward Orton Memorial Lecture Award and 2009 Purdy Award from American Ceramic Society, 2011 MRS Medal from the Materials Research Society, 1999 Burton Medal from Microscopy Society of America.



**Jun Chen** received his B.S. and M.S. in Electrical Engineering from the School of Electronic Information and Communications at Huazhong University of Science and Technology in 2007 and 2010, respectively, and a second M.S. in Biological Engineering from the College of Engineering at The University of Georgia in 2012. He is

currently a Ph.D. candidate in the School of Materials Science and Engineering at The Georgia Institute of Technology, working under the supervision of Prof. Zhong Lin Wang. His research focuses primarily on nanomaterial-based energy harvesting, energy storage, active sensing and self-powered micro-/nano-systems. His H-index is 22.



**Dr. Long Lin** received his B.S. in Materials Science and Engineering from Tsinghua University, China in 2010 and his Ph.D. from Georgia Tech in 2015 under the supervision of Prof. Zhong Lin Wang. His research interests include synthesis of semiconductor nanomaterials, piezoelectric nanogenerators, triboelectric nanogenerators, self-powered systems, and active sensors.

TOC

A review about the principles, novel applications and perspectives of triboelectric nanogenerator as a power source and as self-powered sensor.

